
Conformal Prediction for Time Series with Modern Hopfield Networks

Andreas Auer* Martin Gauch*,† Daniel Klotz* Sepp Hochreiter*

*ELLIS Unit Linz and LIT AI Lab, Institute for Machine Learning,
Johannes Kepler University Linz, Austria

†Google Research, Zürich, Switzerland

Abstract

To quantify uncertainty, conformal prediction methods are gaining continuously more interest and have already been successfully applied to various domains. However, they are difficult to apply to time series as the autocorrelative structure of time series violates basic assumptions required by conformal prediction. We propose HopCPT, a novel conformal prediction approach for time series that not only copes with temporal structures but leverages them. We show that our approach is theoretically well justified for time series where temporal dependencies are present. In experiments, we demonstrate that our new approach outperforms state-of-the-art conformal prediction methods on multiple real-world time series datasets from four different domains.

1 Introduction

Uncertainty estimates are imperative to make actionable predictions for complex time-dependent systems (e.g., Gneiting & Katzfuss, 2014; Zhu & Laptev, 2017). This is particularly evident for environmental phenomena such as flood forecasting (e.g., Krzysztofowicz, 2001), since they exhibit pronounced seasonality. Conformal Prediction (CP, Vovk et al., 1999) provides uncertainty estimates based on prediction intervals. It achieves finite-sample marginal coverage with almost no assumptions, except that the data is exchangeable (Vovk et al., 2005; Vovk, 2012). However, CP for time series is not trivial because temporal dependencies often violate the exchangeability assumption.

HopCPT. For time series models that predict a given system, the errors are typically specific to the input describing the current situation. To apply CP, HopCPT uses continuous Modern Hopfield Networks (MHNs). The MHN uses large weights for past situations that were similar to the current one and weights close to zero for past situations that were dissimilar to the current one (Figure 1). The CP procedure uses the weighted errors to construct strong uncertainty estimates close to the desired coverage level. This exploits that similar situations (which we call a regime) tend to follow the same error distribution. HopCPT achieves new state-of-the-art efficiency, even under non-exchangeability and on large datasets.

Our main contributions are:

1. We propose HopCPT, a CP method for time series, a domain where CP struggled so far.
2. We introduce the concept of error regimes to CP, which softens the excitability requirements and enables efficient CP for time series.
3. HopCPT uses MHN for a similarity-based sample reweighting. In contrast to existing approaches, HopCPT can learn from large datasets and predict intervals at arbitrary coverage levels without retraining.
4. HopCPT achieves state-of-the-art results for conformal time series prediction tasks from various real-world applications.

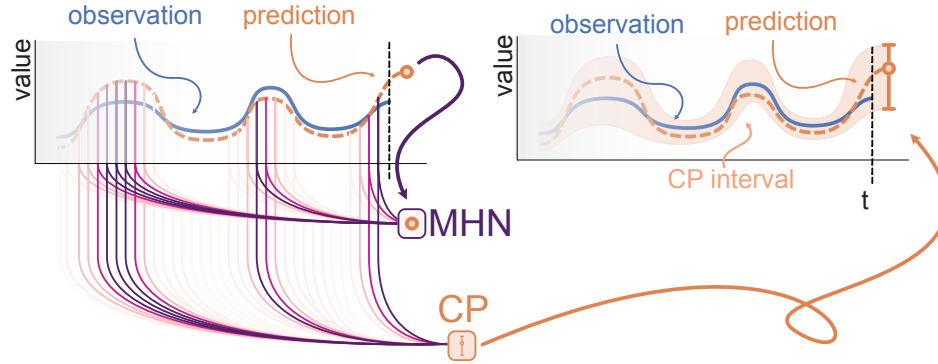


Figure 1: Schematic illustration of HopCPT. The Modern Hopfield Network (MHN) identifies regimes similar to the current one and up-weights them (colored lines). The weighted information enriches the conformal prediction (CP) procedure so that prediction intervals can be derived.

5. HopCPT is the first algorithm with coverage guarantees that was applied to hydrological prediction applications — a domain where uncertainty plays a key role in tasks such as flood forecasting and hydropower management.

1.1 Related Work

Regimes. In a world with non-linear dynamics, different environmental conditions lead to different error characteristics of models that predict based on these conditions. If we do not account for these different conditions, temporal changes may lead to unnecessarily large prediction intervals, i.e., to high uncertainty. For example, solar energy production is high and stable on a sunny day, fluctuates during cloudy days, and is zero at night. Often, the current environmental condition was already observed at previous points in time. The error at these time steps is therefore assumed to have the same distribution as the current error. Following Quandt (1958) and Hamilton (1990), we call the sets of time steps with similar environmental conditions *regimes*. Although conditional CP is in general impossible (Foygel Barber et al., 2021), we show that conditioning on such regimes can lead to better prediction intervals while preserving the specified coverage. Hamilton (1990) models time series regimes as a discrete Markov process and conditions a classical autoregressive model on the regime states. Sanquer et al. (2012) use a smooth transition approach to model multi-regime time series. Tajeuna et al. (2021) propose an approach to discover and model regime shifts in an ecosystem that comprises multiple time series. Further, Masserano et al. (2022) handle distribution shifts by retraining a forecasting model with training data from a non-uniform adaptive sampling. Although these approaches are not in a CP setting, their work is similar in spirit, as they also follow the general idea to condition on parts of the time series with similar regimes.

CP and extensions. For thorough introductions to CP, we refer the reader to the foundational work of Vovk et al. (1999) and a recent introductory paper by Angelopoulos & Bates (2021). There exist a variety of extensions for CP that go “beyond exchangeability” (Vovk et al., 2005). For example, Papadopoulos & Haralambous (2011) apply CP to a nearest neighbor regression setting, Teng et al. (2022) apply CP to the feature space of models, Angelopoulos et al. (2020) use CP to generate uncertainty sets for image classification tasks, and Toccaceli et al. (2017) use a label-conditional variant to apply CP to biological activity prediction. Of specific interest to us is the research regarding non-exchangeable data of Tibshirani et al. (2019) and Foygel Barber et al. (2022). Both handle potential shifts between the calibration and test set by reweighting the data points. Tibshirani et al. (2019) restrict themselves to settings with full knowledge about the change in distribution; Foygel Barber et al. (2022) rely on fixed weights. In our work, we refrain from this assumption because such information is typically not available in time series prediction. Another important research direction is the work on normalized conformity scores (see Fontana et al., 2023, and references therein). In this setting, the goal is to adapt the conformal bounds through a scaling factor in the nonconformity function. The work on normalized conformity scores does not explicitly tailor their approaches to time series.

CP for time series. Gibbs & Candes (2021) and Zaffran et al. (2022) account for shifts in sequential data by continuously adapting an internal coverage target. Adaption-based approaches like these are orthogonal to HopCPT and can serve as an enhancement. Stankevičiūtė et al. (2021) use CP in conjunction with recurrent neural networks in a multi-step prediction setting, assuming that the series of observations is independent. Thus, no weighting of the scores is required. Sun & Yu (2022) introduce CopulaCPTS which applies CP to time series with multivariate targets. They conformalize their prediction based on a copula of the target variables and adapt their calibration set in each step. Jensen et al. (2022) use a bootstrap ensemble to enable CP on time series. NexCP (Foygel Barber et al., 2022) uses exponential decay as the weighting method, arguing that the recent past is more likely to be of the same error distribution. HopCPT can learn this strategy, but does not a priori commit to it. Xu & Xie (2022a) propose EnbPI, which uses quantiles of the k most recent errors for the prediction interval. Additionally, they introduce a novel leave-one-out ensembling technique. This is specifically geared to settings with scarce data and difficult to use for larger datasets, which is why we do not apply it in our experiments. EnbPI is designed around the notion that near-term errors are often independent and identically distributed and therefore exchangeable. SPCI (Xu & Xie, 2022b) softens this requirement by exploiting the autocorrelative structure with a random forest. However, it re-calculates the random forest model at each time step, which is a computational burden that prohibits its application to large datasets. Our approach relaxes the requirement even further, as we do not assume that the data for the interval computations pertains to the k most recent errors.

Non-CP methods Beside CP there exist a wide range of approaches for uncertainty-aware time series prediction. For example, Mixture Density Networks (Bishop, 1994) directly estimate the parameters of a mixture of distributions. However, they require a distribution assumption and do not provide any theoretical guarantees. Gaussian Processes (e.g., Zhu et al., 2023; Corani et al., 2021; Sun et al., 2022) model time series by calculating posterior functions based on the samples and a prior but are computationally limited for large and high dimensional datasets.

Continuous Modern Hopfield Networks. MHN are energy-based associative memory networks. They advance conventional Hopfield Networks (Hopfield, 1982) by introducing continuous queries and states via a new energy function. The new energy function leads to exponential storage capacity, while retrieval is possible with a one-step update (Ramsauer et al., 2021). Examples for successful applications of MHN are Widrich et al. (2020); Fürst et al. (2022); Dong et al. (2022); Sanchez-Fernandez et al. (2022); Paischer et al. (2022); Schäfl et al. (2022); and Xu et al. (2022). MHN are related to Transformers (Vaswani et al., 2017) as their attention mechanism is closely related to the association mechanism in MHN. In fact, Ramsauer et al. (2021) show that Transformers attention is a special case of the MHN association, at which we arrive when the queries and states are mapped to an associative Hopfield space with the dimensions d_k , and the inverse softmax temperature is set to $\beta = \frac{1}{\sqrt{d_k}}$. However, we use the framework of MHN because we want to highlight the associative memory mechanism as HopCPT directly ingests encoded observations. This perspective further allows HopCPT to update the memory for each new observation. For more details, we refer to Appendix H in the supplementary material.

1.2 Setting

Our setting consists of a multivariate time series $\{(\mathbf{x}_t, y_t)\}$, $t = 1, \dots, T$, with a feature vector $\mathbf{x}_t \in \mathbb{R}^m$, a target variable $y_t \in \mathbb{R}$, and a given black-box prediction model $\hat{\mu}$ that generates a point prediction $\hat{y}_t = \hat{\mu}(\mathbf{X}_t)$. The input feature matrix \mathbf{X}_{t+1} can include all previous and current feature vectors $\{\mathbf{x}_i\}_{i=1}^{t+1}$, as well as all previous targets $\{y_i\}_{i=1}^t$. Our goal is to construct a corresponding prediction interval $\hat{C}_t^\alpha(\mathbf{Z}_{t+1})$ — a set that includes y_{t+1} with at least a specified probability $1 - \alpha$. In its basic form, \mathbf{Z}_{t+1} will only contain \hat{y}_{t+1} , but it can also inherit \mathbf{X}_{t+1} or other useful features. Following Vovk et al. (2005), we define the *coverage* as

$$\Pr \left\{ Y_{t+1} \in \hat{C}_t^\alpha(\mathbf{Z}_{t+1}) \right\} \geq 1 - \alpha, \quad (1)$$

where Y_{t+1} is the random variable of the prediction. An infinitely wide prediction interval is 100% reliable, but not informative of the uncertainty. Thus, CP aims to minimize the width of the prediction interval \hat{C}_t^α , while preserving the coverage. A smaller prediction interval is called a more *efficient* interval (Vovk et al., 2005) and usually evaluated as the mean of the interval width over the prediction period (*PI-Width*).

Standard split conformal prediction takes a calibration set of size n which has not been used to train the prediction model $\hat{\mu}$. For each data sample, it calculates the so-called non-conformity score (Vovk et al., 2005). In a regression setting, this score often simply corresponds to the absolute error of the prediction (e.g., Foygel Barber et al., 2022). The prediction interval is then calculated based on the empirical $1 - \alpha$ quantile $Q_{1-\alpha}$ of the calibration scores:

$$\widehat{C}_n^\alpha(\mathbf{Z}_{t+1}) = \hat{\mu}(\mathbf{X}_{t+1}) \pm Q_{1-\alpha}(\{|y_i - \hat{\mu}(\mathbf{X}_i)|\}_{i=1}^n). \quad (2)$$

If the data is exchangeable and $\hat{\mu}$ treats the data points symmetrically, the errors on the test set follow the distribution from the calibration. Hence, the empirical quantiles on the calibration and test set will be approximately equal and it is guaranteed that the interval provides the desired coverage.

The *actual marginal miscoverage* α^* is based on the observed samples of a test set. If the *specified miscoverage* α differs from the α^* in the evaluation, we denote the difference as the coverage gap $\Delta \text{Cov} = \alpha - \alpha^*$.

The remainder of this manuscript is structured as follows: In Section 2, we present HopCPT alongside a theoretical motivation and a synthetic example that demonstrates the advantages of the approach. In Section 3, we evaluate the performance against state-of-the-art CP approaches and discuss the results. Section 4 gives our conclusions and provides an outlook on potential future work.

2 HopCPT

HopCPT¹ combines conformal-style quantile estimation with learned similarity-based MHN retrieval.

2.1 Theoretical Motivation

The theoretical motivation for the MHN retrieval stems from Foygel Barber et al. (2022), who introduced CP with weighted quantiles. In the split conformal setting, the according prediction interval is calculated as

$$\widehat{C}_t^\alpha(\mathbf{X}_{t+1}) = \hat{\mu}(\mathbf{X}_{t+1}) \pm Q_{1-\alpha} \left(\sum_{i=1}^t a_i \delta_{\epsilon_i} + a_{t+1} \delta_{+\infty} \right), \quad (3)$$

where $\hat{\mu}$ represents an existing point prediction model, Q_τ is the τ -quantile of a distribution, and δ_{ϵ_i} is a point mass at $|\epsilon_i|$ (i.e., a probability distribution with all its mass at $|\epsilon_i|$), where ϵ_i are the errors of the existing prediction model defined by $\epsilon_i = y_i - \hat{\mu}(\mathbf{X}_i)$. The normalized weight a_i of data sample i is

$$a_i = \begin{cases} \frac{1}{\omega_1 + \dots + \omega_{t+1}} & \text{if } i = t + 1, \\ \frac{\omega_i}{\omega_1 + \dots + \omega_{t+1}} & \text{else,} \end{cases} \quad (4)$$

where ω_i are the un-normalized weights of the samples. In the case of $\omega_1 = \dots = \omega_t = 1$, this corresponds to standard split CP. Given this framework, Foygel Barber et al. (2022) show that ΔCov can be bounded in a non-exchangeable data setting: Let $D = ((\mathbf{X}_1, Y_1), \dots, (\mathbf{X}_{t+1}, Y_{t+1}))$ be a dataset where the last entry represents the test sample, and D^i be a permutation of D which exchanges the test sample at $t + 1$ with the i -th sample. Then, ΔCov can be bounded from below by the weighted sum of the total variation distances d_{TV} between these permutations:

$$\Delta \text{Cov} \geq - \sum_{i=1}^t a_i \cdot d_{\text{TV}}(D, D^i) \quad (5)$$

If D is a composite of multiple regimes and the test sample is from the same regime as the calibration sample i , then the distance between D and D^i is small. Conversely, the distance might be big if the calibration sample is from a different regime. In HopCPT, the MHN association resembles direct estimates of a_i — dynamically assigning high values to samples from similar regimes.

Appendix B provides an extended theoretical discussion that relates HopCPT to the work of Foygel Barber et al. (2022) and Xu & Xie (2022a), who provide the basis for our theoretical

¹<https://github.com/ml-jku/HopCPT>

analyses of the CP interval. The latter compute individual quantiles for the upper and lower bound of the prediction interval on the errors themselves, in contrast to standard CP which uses only the highest absolute error quantile. This can provide more efficient intervals in case $E[\epsilon] \neq 0$ within the corresponding error distribution. Applying this principle to HopCPT where the error distribution is conditional to the error regime and assuming that HopCPT can successfully identify these regimes (Appendix: Assumption B.3), we arrive at a conditional asymptotic coverage bound (Appendix: Theorem B.8) and an asymptotic marginal coverage bound (Appendix: Theorem B.9).

2.2 Associative Soft-selection for CP

We use a MHN to identify parts of the time series where the conditional error distribution is similar: For time step $t + 1$, we query the memory of the past and look for matching patterns. The MHN then provides an association vector \mathbf{a}_{t+1} that allows to soft-select the relevant periods of the memory. The selection procedure is analogous to a k -nearest neighbor classifier for hard selection, but it has the advantage that the similarity measure can be learned. Formally, the soft-selection is defined as:

$$\mathbf{a}_{t+1} = \text{softmax}(\beta m(\mathbf{Z}_{t+1}) \mathbf{W}_q \mathbf{W}_k m(\mathbf{Z}_{1:t})), \quad (6)$$

where m is an encoding network (Section 2.3) that transforms the raw time series features of the current step \mathbf{Z}_{t+1} to the query pattern and the memory $\mathbf{Z}_{1:t}$ to the stored key patterns; \mathbf{W}_q and \mathbf{W}_k are the learned transformations which are applied before associating the query with the memory; β is a hyperparameter that controls the softmax temperature. As mentioned above, HopCPT uses the softmax to amplify the impact of the data samples that are likely to follow a similar error distribution and to reduce the impact of samples that follow different distributions (see Section 2.1). This error weighting leads not only to more efficient prediction intervals in our experiments, but can also reduce the miscoverage (Section 3.2).

With the soft-selected time steps we can derive the CP interval using the observed errors ϵ . Following Xu & Xie (2022a), we use individual quantiles for the upper and lower bound of the prediction interval, calculated from the errors themselves. HopCPT computes the prediction interval \hat{C}_t^α for time step $t + 1$ in the following way:

$$\hat{C}_t^\alpha(\mathbf{Z}_{t+1}) = \left[\hat{\mu}(\mathbf{X}_{t+1}) + q\left(\frac{\alpha}{2}, \mathbf{Z}_{t+1}\right), \hat{\mu}(\mathbf{X}_{t+1}) + q\left(1 - \frac{\alpha}{2}, \mathbf{Z}_{t+1}\right) \right], \quad (7)$$

where $q(\tau, \mathbf{Z}_{t+1}) = \mathbf{Q}_\tau(E_{t+1})$ and E_{t+1} is a multiset created by drawing n times from $[\epsilon_i]_{i=1}^t$ with corresponding probabilities $[a_{t+1,i}]_{i=1}^t$.

2.3 Encoding Network

We embed \mathbf{Z}_t using a 2-layer fully connected network m^L with ReLU activations and enhance the representation by temporal encoding features $z_{T,t}^{\text{time}}$. The full encoding network can be represented as $m(\mathbf{Z}_t) = [m^L(\mathbf{Z}_t) \parallel z_{T,t}^{\text{time}}]$, where $z_{T,t}^{\text{time}}$ is a simple temporal encoding that makes time dependent notions of similarity learnable (e.g., the windowed approach of EnbPI or the exponentially decaying weighting scheme of NexCP). Specifically, we use $z_{T,t}^{\text{time}} = \frac{t}{T}$. In general, we find that our method is not very sensitive to the exact encoding strategy (e.g., number of layers), which is why we kept to a simple choice throughout all experiments.

2.4 Training Procedure

We partition the split conformal calibration data into training and validation sets. Training MHN with quantiles is difficult, which is why we use an auxiliary task: Instead of applying the association mechanism from Equation 6 directly, we use the absolute errors as the value patterns of the MHN. This way, the MHN learns to align errors from time steps with similar regime properties. Intuitively, the observed errors from these time steps should work best to predict the current absolute error. We use the mean squared error as loss function (Equation 8). To allow for efficient training, we simultaneously calculate the association of all T time steps within a training split with each other. We mask the association from a time step to itself. The resulting association from each step to each step is $\mathbf{A}_{1:T,1:T}$, and the loss function \mathcal{L} is

$$\mathcal{L} = T^{-1} * \|(|\epsilon_{1:T}| - \mathbf{A}_{1:T,1:T} |\epsilon_{1:T}|)\|_1. \quad (8)$$

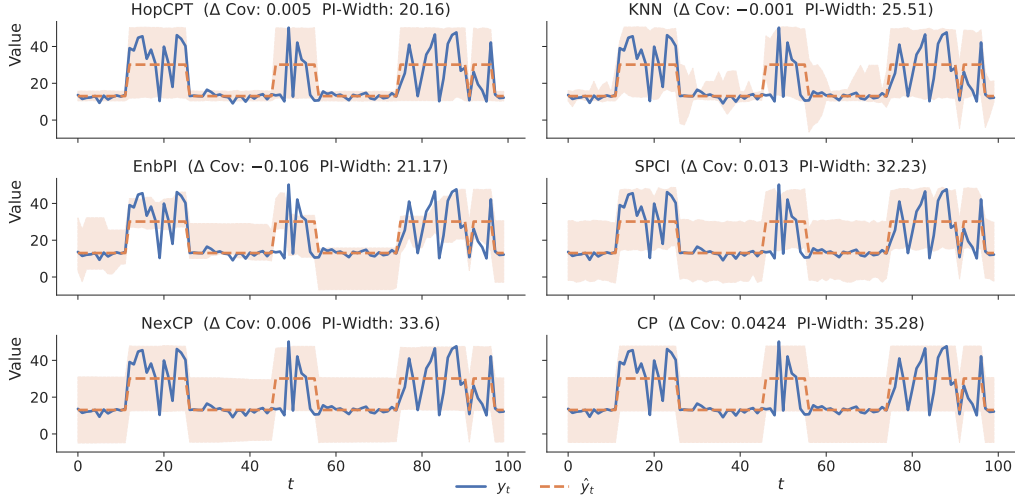


Figure 2: Synthetic example evaluation. HopCPT has the smallest prediction interval width (PI-width), while maintaining the warranted coverage (i.e., a Δ Cov that is positive and close to zero).

This incentivizes the network to learn a representation such that the resulting soft-selection focuses on time steps with a similar error distribution. Alternatively, one could use a loss based on sampling from the softmax. This would correspond more closely to the inference procedure. However, it makes training less efficient because each training step only carries information about a single value of ϵ_i . In contrast, \mathcal{L} leads to more sample-efficient training. Choosing \mathcal{L} assumes that it leads to a retrieval of errors from appropriate regimes instead of mixing unrelated errors. Section 3.2 and Appendix A.3 provide evidence that this holds empirically.

2.5 Synthetic Example

The following synthetic example illustrates the advantages of the HopCPT association mechanism. We model a bivariate time series $D = \{(x_t, y_t)\}_{t=1}^T$. While y_t serves as the target variable, x_t represents the feature in our prediction. The series is composed of two different regimes: target values are generated by $y_t = 10 + x_t + \mathcal{N}(0, \frac{x_t}{2})$ or $y_t = 10 + x_t + U(-x_t, x_t)$. x_t is constant within a regime ($x = 3$ and $x = 21$, respectively). The regimes alternate. For each regime, we sample the number of time steps from the discrete uniform distribution $\mathcal{U}(1, 25)$. We create 1,000 time steps and split the data equally into training, calibration, and test sets. We use a ridge regression model as prediction model $\hat{\mu}$. HopCPT can identify the time steps of relevant regimes and therefore creates efficient prediction intervals while still preserving the coverage (Figure 2). EnbPI, SPCI, and NexCP focus only on the recent time steps and thus fail to base their intervals on information from the correct regime. Whenever the regime changes from small to high errors, EnbPI propagates the small error signal and therefore loses coverage. Similarly, its prediction intervals for the small error regime are inefficient (Figure 2, row 3). SPCI, NexCP, and standard CP cannot properly select the relevant time steps, either. They do not lose coverage, but produce wide intervals for all time steps (Figure 2, rows 4 and 5). Lastly, if we replace the MHN with a kNN, it can retrieve information from similar regimes. However, its naive retrieval mechanism fails to focus on the informative features because it cannot learn them (Figure 2, row 2).

2.6 Limitations

HopCPT builds upon the formal guarantees of CP, but it is able to relax the data exchangeability assumption of CP which are problematic for time series data. That said, HopCPT still relies on assumptions on how it learns to identify the respective error regimes and exchangeability within regimes (see Section 2.1 and Appendix B). Our extensive empirical evaluation suggests that these assumptions hold in practice. HopCPT is generally well-suited for very long time series because the memory requirement in the inference scales only linearly with the memory size. Nevertheless, for extremely large datasets it can be the case that not all historical time steps may be kept in the Hopfield memory

anymore. HopCPT can, similar to existing methods, disregard time steps by removing the oldest entries from the memory, or alternatively use a sub-sampling strategy. On the other hand, for datasets with very scarce data it might be difficult to learn a useful embedding of the time steps. In that case, it could be better to use kNN rather than learning the similarity with MHN (Appendix D). Additional considerations regarding the potential social impact of the method are summarized in Appendix I.

3 Experiments

This section provides a comparative evaluation of HopCPT and analyzes its association mechanism.

3.1 Setup

Datasets. We use datasets from four different domains: (a) Three solar radiation datasets from the US National Solar Radiation Database (Sengupta et al., 2018). The smallest one consists of 8 time series from different locations over a period of 84 days. This dataset is also used in Xu & Xie (2022a,b). In addition, we evaluate on a 1-year and a 3-year dataset, with 50 time series each. (b) An air quality dataset from Beijing, China (Zhang et al., 2017). It consists of 12 time series, each from a different measurement station, over a period of 4 years. The dataset has two prediction targets, the PM10 (as in Xu & Xie, 2022a,b) and PM2.5 concentrations, which we evaluate separately. (c) Sap flow² measurements from the Sapfluxnet data project (Poyatos et al., 2021). Since the individual measurement series are considerably heterogeneous in length, we use a subset of 24 time series, each with between 15,000 and 20,000 data points and varying sampling rates. (d) Streamflow, a dataset of water flow measurements and corresponding meteorologic observations from 531 rivers across the continental United States (Newman et al., 2015; Addor et al., 2017). The measurements span 28 years at a daily time scale. For more detailed information about the datasets see Appendix C.

Prediction models. We use four prediction models for the solar radiation, the air quality, and the sap flux datasets to ensure that our results generalize: a random forest, a LightGBM, a ridge regression, and a Long Short-Term Memory (LSTM) (LSTM; Hochreiter & Schmidhuber, 1997) model. For the former three models we follow the related work (Xu & Xie, 2022a,b; Foygel Barber et al., 2022) and train a separate prediction model for each individual time series. The random forest and LightGBM models are implemented with the darts library (Herzen et al., 2022), the ridge regression model with sklearn (Pedregosa et al., 2011). For the LSTM model, we instead train a global model on all time series of a dataset, as is standard for state-of-the-art deep learning models (e.g., Oreshkin et al., 2020; Salinas et al., 2020; Smyl, 2020). The LSTM is implemented with PyTorch (Paszke et al., 2019). For the streamflow dataset, we deviate from this scheme and instead only use the state-of-the-art model, which is also an LSTM network (Kratzert et al., 2021, see Appendix C).

Compared approaches. We compare HopCPT to different state-of-the-art CP approaches for time series data: EnbPI (Xu & Xie, 2022a), SPCI (Xu & Xie, 2022b), NexCP (Foygel Barber et al., 2022), CopulaCPTS (Sun & Yu, 2022), and AdaptiveCI³ (Gibbs & Candes, 2021). In addition, the results of standard split CP (CP) serve as a baseline, which, for the LSTM base predictor, corresponds to CF-RNN (Stankevičiūtė et al., 2021) in our setting (one-step, univariate target variable). Appendix A.1 describes our hyperparameter search for each method. For SPCI, an adaption of the original algorithm was necessary to provide scalability to larger datasets. Appendix A.2 contains more details and an empirical justification. Appendix G evaluates the addition of AdaptiveCI (Gibbs & Candes, 2021) as an enhancement to HopCPT and the other time series CP methods. Appendix A.3 gives a comparison to non-CP methods. Lastly, Appendix D presents a supplemental comparison to kNN that shows the superiority of the learned similarity representation in HopCPT.

²Sap flow refers to the movement of water within a plant. In the environmental sciences, it is commonly used as a proxy for plant transpiration.

³AdaptiveCI works on top of an existing quantile prediction method. Hence, we exclusively make comparisons based on the LightGBM models that can predict quantiles instead of point estimates. The approach is orthogonal to the remaining compared models and could be combined with HopCPT.

Table 1: Performance of the evaluated CP algorithms for the Solar (3Y), Air Quality (10PM), Sap flow, and Streamflow (SF) datasets. The specified miscoverage level is $\alpha = 0.1$ for all experiments. The column FC specifies the prediction algorithm used for the experiment (Forest: Random Forest, LGBM: LightGBM, Ridge: Ridge Regression, LSTM: LSTM neural network). Bold numbers correspond to the best result for the respective metric in the experiment (PI-Width and Winkler score), given that $\Delta\text{Cov} \geq -0.25\alpha$, i.e., the specific algorithm reached at least approximate coverage (the result is grayed otherwise). The error term represents the standard deviation over repeated runs with different seeds (results without an error term are from deterministic models).

		UC	HopCPT	SPCI	EnbPI	NexCP	CopulaCPTS	CP/CF-RNN	AdaptiveCI
Solar 3Y	Forest	ΔCov	0.029 \pm 0.012	0.012 \pm 0.000	-0.031	-0.002	0.005	0.004	
		PI-Width	39.0 \pm 6.2	103.1 \pm 0.1	131.1	166.6	174.9	174.6	
		Winkler	0.73 \pm 0.20	1.74 \pm 0.00	2.47	2.53	2.75	2.76	
	LGBM	ΔCov	0.001 \pm 0.003	0.014 \pm 0.000	-0.023	-0.002	0.006	0.006	0.001
		PI-Width	37.7 \pm 0.7	102.2 \pm 0.1	133.6	159.9	169.8	170.2	67.1
		Winkler	0.57 \pm 0.01	1.75 \pm 0.00	2.52	2.55	2.80	2.81	1.19
	Ridge	ΔCov	0.040 \pm 0.001	0.002 \pm 0.000	-0.074	-0.001	0.004	0.005	
		PI-Width	44.9 \pm 0.5	108.2 \pm 0.0	131.1	171.0	166.0	167.7	
		Winkler	0.64 \pm 0.00	1.82 \pm 0.00	2.49	2.66	2.73	2.74	
	LSTM	ΔCov	0.001 \pm 0.006	0.014 \pm 0.000	-0.018	-0.001	0.007	0.007	
		PI-Width	17.9 \pm 0.6	27.8 \pm 0.0	24.6	28.2	31.9	33.0	
		Winkler	0.30 \pm 0.01	0.62 \pm 0.00	0.64	0.63	0.68	0.70	
Air 10 PM	Forest	ΔCov	0.028 \pm 0.019	0.008 \pm 0.000	-0.066	-0.004	-0.019	-0.033	
		PI-Width	93.9 \pm 11.1	118.5 \pm 0.1	202.8	263.5	243.1	229.8	
		Winkler	1.50 \pm 0.09	2.23 \pm 0.00	4.16	4.03	4.94	4.98	
	LGBM	ΔCov	0.017 \pm 0.016	0.023 \pm 0.000	-0.057	-0.004	-0.017	-0.028	-0.001
		PI-Width	85.6 \pm 7.4	113.2 \pm 0.1	178.3	224.8	206.7	196.5	186.4
		Winkler	1.45 \pm 0.06	1.94 \pm 0.00	3.69	3.64	4.33	4.36	3.00
	Ridge	ΔCov	0.010 \pm 0.007	0.024 \pm 0.000	-0.045	-0.002	0.010	0.012	
		PI-Width	79.9 \pm 4.7	93.9 \pm 0.1	120.0	153.3	153.7	155.3	
		Winkler	1.35 \pm 0.06	1.52 \pm 0.00	2.60	2.68	2.95	2.96	
	LSTM	ΔCov	-0.002 \pm 0.005	0.010 \pm 0.000	-0.025	-0.002	0.001	0.004	
		PI-Width	62.7 \pm 1.5	62.2 \pm 0.0	58.1	62.4	61.8	63.0	
		Winkler	1.33 \pm 0.01	1.21 \pm 0.00	1.32	1.29	1.34	1.34	
Sap flow	Forest	ΔCov	0.009 \pm 0.019	0.007 \pm 0.000	-0.042	0.000	0.014	0.005	
		PI-Width	1078.7 \pm 73.7	1741.8 \pm 2.4	3671.6	6137.1	7131.1	7201.5	
		Winkler	0.30 \pm 0.01	0.59 \pm 0.00	1.24	1.56	1.76	1.80	
	LGBM	ΔCov	-0.016 \pm 0.013	0.003 \pm 0.000	-0.040	-0.003	0.006	-0.007	0.010
		PI-Width	875.5 \pm 49.8	1582.3 \pm 1.0	2924.1	4805.3	5588.5	5614.8	6273.5
		Winkler	0.27 \pm 0.00	0.49 \pm 0.00	0.96	1.25	1.43	1.46	1.50
	Ridge	ΔCov	-0.025 \pm 0.023	-0.241 \pm 0.000	-0.041	-0.015	-0.251	-0.358	
		PI-Width	1639.6 \pm 93.2	2060.5 \pm 1.6	3117.5	10628.9	8943.3	7148.7	
		Winkler	0.46 \pm 0.05	2.52 \pm 0.00	0.92	2.42	3.31	5.85	
	LSTM	ΔCov	0.004 \pm 0.004	0.004 \pm 0.000	-0.019	-0.000	-0.022	-0.042	
		PI-Width	594.3 \pm 7.7	628.2 \pm 0.9	768.0	990.0	903.9	817.2	
		Winkler	0.19 \pm 0.01	0.24 \pm 0.00	0.28	0.32	0.35	0.36	
SF	LSTM	ΔCov	0.001 \pm 0.041	0.027 \pm 0.000	-0.054	-0.000	0.005	0.009	
		PI-Width	1.39 \pm 0.17	1.58 \pm 0.00	1.55	1.94	1.99	2.08	
		Winkler	0.79 \pm 0.03	0.91 \pm 0.00	1.27	1.21	1.28	1.29	

Metrics. In our analyses, we compute Δ Cov, PI-Width, and the Winkler score (Winkler, 1972) per time series and miscoverage level. The Winkler score jointly elicitates miscoverage and interval width in a single metric:

$$\text{WS}_\alpha(\mathbf{Z}_{t+1}, y_{t+1}) = \begin{cases} \text{IW}_t^\alpha(\mathbf{Z}_{t+1}) + \frac{2}{\alpha}(y_{t+1} - \widehat{C}_t^{\alpha,u}(\mathbf{Z}_{t+1})) & \text{if } y_{t+1} > \widehat{C}_t^{\alpha,u}(\mathbf{Z}_{t+1}), \\ \text{IW}_t^\alpha(\mathbf{Z}_{t+1}) + \frac{2}{\alpha}(\widehat{C}_t^{\alpha,l}(\mathbf{Z}_{t+1}) - y_{t+1}) & \text{if } y_{t+1} < \widehat{C}_t^{\alpha,l}(\mathbf{Z}_{t+1}), \\ \text{IW}_t^\alpha(\mathbf{Z}_{t+1}) & \text{else.} \end{cases} \quad (9)$$

The score is calculated per time step t and miscoverage level α . It corresponds to the interval width $\text{IW}_t^\alpha = \widehat{C}_t^{\alpha,u} - \widehat{C}_t^{\alpha,l}$ whenever the observed value y_t is between the upper bound $\widehat{C}_t^{\alpha,u}(\mathbf{Z}_{t+1})$ and the lower bound $\widehat{C}_t^{\alpha,l}(\mathbf{Z}_{t+1})$ of $\widehat{C}_t^\alpha(\mathbf{Z}_{t+1})$. If y_{t+1} is outside these bounds, a penalty is added to the interval width. We evaluate the mean Winkler score over all time steps.

We repeated each experiment with 12 different seeds. For brevity, we only show the mean performance of one dataset per domain for $\alpha = 0.1$ in the main paper (which is the most commonly reported value in the CP literature; e.g., Xu & Xie, 2022b; Foygel Barber et al., 2022; Gibbs & Candes, 2021). Appendix A.3 presents additional results for all datasets and more α levels.

3.2 Results & Discussion

HopCPT has the most efficient prediction intervals for each domain — with only one exception (Table 1; significance tested with a Mann–Whitney U test at $p < 0.005$) for the evaluated miscoverage level ($\alpha = 0.1$). In multiple experiments (Solar (3Y), Solar (1Y)), the HopCPT prediction intervals are less than half as wide as those of the approach with the second-smallest PI-Width. The second-most efficient intervals are predicted most often by SPCI. This ranking also holds for the Winkler score, where HopCPT achieves the best (i.e., lowest) Winkler scores and SPCI ranks second in most experiments. Notably, these results reflect the increasing requirements posed by each uncertainty estimation method on the dataset (Section 1.1).

Furthermore, HopCPT outperforms the other methods regarding both Winkler score and PI-Width when we evaluate over additional datasets and at different miscoverage levels (see Appendix A.3). HopCPT is the best-performing approach in the vast majority of cases. The variation in size of the different solar datasets (results for Solar (1Y) and Solar (3M) in Appendix A.3) shows that HopCPT especially increases its lead when more data is available. We hypothesize that this is because the MHN can learn more generalizable retrieval patterns with more data. However, data scarcity is not a limitation of similarity-based CP in general. In fact, a simplified and almost parameter-free variation of HopCPT, which replaces the MHN with kNN retrieval, performs best on the smallest solar dataset, as we demonstrate in Appendix D.

Most approaches have a coverage gap close to zero in almost all experiments — they approximately achieve the specified marginal coverage level. This is also reflected by the fact that the ranking of Winkler scores and PI-Widths agree in most evaluations. Appendix A.4 provides a supplementary analysis of the local coverage. The results for non-CP methods show a different picture (see Appendix A.3 and Table 7). Here, the non-CP models most often exhibit very narrow prediction intervals at the cost of high miscoverage.

Interestingly, standard CP also achieves good coverage for all experiments at the cost of inefficient prediction intervals. There is one notable exception: for the Sap flow dataset with ridge regression, we find Δ Cov = -0.358 . In this case, we argue that the bad performance of standard CP is driven by a strong violation of the (required) exchangeability assumption. Specifically, a trend in the errors leads to a distribution shift over time (as illustrated in Appendix A.3, Figure 4). HopCPT and NexCP handle this shift without substantial loss in coverage. The inferior coverage of SPCI is likely influenced by the modification to larger datasets (see Appendix A.2).

Performance gaps between the approaches differ considerably across datasets, but are generally consistent across prediction models. The biggest differences between the best and worst methods exist in Solar (3Y) and Sap flow, likely due to the distinctive regimes in these datasets. The smallest (but still significant) differences are visible in the Streamflow data. On this dataset, we also evaluated the state-of-the-art non-CP uncertainty model in the domain (Klotz et al., 2022, see Appendix A.3) and found that HopCPT outperforms it with respect to efficiency.

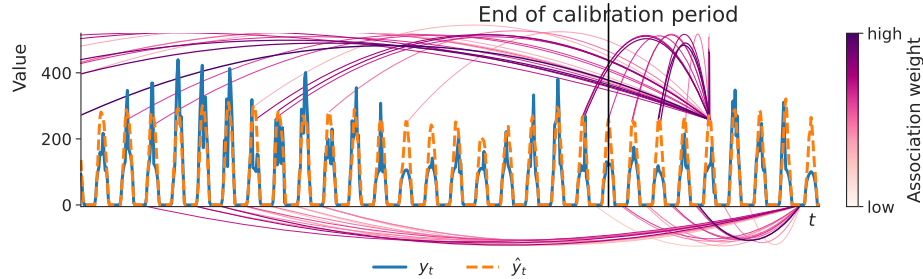


Figure 3: Exemplary visualization of the 30 highest association weights that the MHN places on previous time steps (some are before the visualized part of the memory). HopCPT retrieves similar peak values when estimating at a peak, and it retrieves similar small values when estimating at a small value.

In terms of computational resources, SPCI is most demanding followed by HopCPT, as both methods require a learning step in contrast to the other methods. A detailed overview can be found in Appendix A.6.

To assess whether HopCPT learns meaningful associations within regimes, we conducted a qualitative study on the Solar (3Y) dataset. Figure 3 shows that HopCPT retrieves the most highly weighted errors from time steps with similar regimes. The illustrated weighting at the time step with a low prediction value retrieves previous time steps which are also in low-valued regimes. Similarly, Figure 5 (Appendix A.3) suggests that the learned distinction corresponds to the error regimes, which is crucial for HopCPT.

4 Conclusions

We have introduced HopCPT, a novel CP approach for time series tasks. HopCPT uses continuous Modern Hopfield Networks to construct prediction intervals based on previously seen events with similar error distribution regimes. We exploit that similar features lead to similar errors. Associating features with errors identifies regimes with similar error distributions. HopCPT learns this association in the Modern Hopfield Network, which dynamically adjusts its focus on stored previous features according to the current regime.

Our experiments with established and novel datasets show that HopCPT achieves state of the art: It generates more efficient prediction intervals than existing CP methods and approximately preserves coverage, even in non-exchangeable scenarios like time series. HopCPT comes with formal guarantees within the CP framework for uncertainty estimation in real-world applications such as streamflow prediction. Furthermore, HopCPT scales well to large datasets, provides multiple coverage levels after calibration, and shares information across individual time series within a dataset.

Future work comprises: (a) Drawing from multiple time series during the inference phase. HopCPT is already trained on the whole dataset at once, but it might be advantageous to leverage more information during inference as well. (b) Investigating direct training objectives from which learning-based CP might benefit. (c) Using HopCPT beyond time series, as non-exchangeability is also an issue in other domains which limits the applicability of existing CP methods.

Acknowledgements

We would like to thank Angela Bitto-Nemling for discussions during the development of the method. The ELLIS Unit Linz, the LIT AI Lab, the Institute for Machine Learning, are supported by the Federal State Upper Austria. We thank the projects AI-MOTION (LIT-2018-6-YOU-212), DeepFlood (LIT-2019-8-YOU-213), Medical Cognitive Computing Center (MC3), INCONTROL-RL (FFG-881064), PRIMAL (FFG-873979), S3AI (FFG-872172), DL for GranularFlow (FFG-871302), EPILEPSIA (FFG-892171), AIRI FG 9-N (FWF-36284, FWF-36235), AI4GreenHeatingGrids(FFG- 899943), INTEGRATE (FFG-892418), ELISE (H2020-ICT-2019-3 ID: 951847), Stars4Waters (HORIZON-CL6-2021-CLIMATE-01-01). We thank Audi.JKU Deep Learning Center, TGW LOGISTICS GROUP GMBH, Silicon Austria Labs (SAL), FILL Gesellschaft mbH, Anyline

GmbH, Google, ZF Friedrichshafen AG, Robert Bosch GmbH, UCB Biopharma SRL, Merck Healthcare KGaA, Verbund AG, GLS (Univ. Waterloo) Software Competence Center Hagenberg GmbH, TÜV Austria, Frauscher Sensoic, TRUMPF and the NVIDIA Corporation. The computational results presented have been achieved in part using the Vienna Scientific Cluster (VSC) and the In-Memory Supercomputer MACH-2 (operated by the Scientific Computing Administration of JKU Linz).

References

- Abbott, L. F. and Arian, Y. Storage capacity of generalized networks. *Physical Review A*, 36: 5091–5094, 1987. doi: 10.1103/PhysRevA.36.5091.
- Addor, N., Newman, A. J., Mizukami, N., and Clark, M. P. The CAMELS data set: catchment attributes and meteorology for large-sample studies. *Hydrology and Earth System Sciences (HESS)*, 21(10):5293–5313, 2017.
- Angelopoulos, A., Bates, S., Malik, J., and Jordan, M. I. Uncertainty sets for image classifiers using conformal prediction. *arXiv preprint arXiv:2009.14193*, 2020.
- Angelopoulos, A. N. and Bates, S. A gentle introduction to conformal prediction and distribution-free uncertainty quantification. *arXiv preprint arXiv:2107.07511*, 2021.
- Baldi, P. and Venkatesh, S. S. Number of stable points for spin-glasses and neural networks of higher orders. *Physical Review Letters*, 58:913–916, 1987. doi: 10.1103/PhysRevLett.58.913.
- Bishop, C. M. Mixture density networks. Technical report, Neural Computing Research Group, 1994.
- Caputo, B. and Niemann, H. Storage capacity of kernel associative memories. In *Proceedings of the International Conference on Artificial Neural Networks (ICANN)*, pp. 51–56, Berlin, Heidelberg, 2002. Springer-Verlag.
- Chen, H. H., Lee, Y. C., Sun, G. Z., Lee, H. Y., Maxwell, T., and Giles, C. L. High order correlation model for associative memory. *AIP Conference Proceedings*, 151(1):86–99, 1986. doi: 10.1063/1.36224.
- Corani, G., Benavoli, A., and Zaffalon, M. Time series forecasting with gaussian processes needs priors. In *Joint European Conference on Machine Learning and Knowledge Discovery in Databases*, pp. 103–117. Springer, 2021.
- Dong, Z., Chen, Z., and Wang, Q. Retrosynthesis prediction based on graph relation network. In *2022 15th International Congress on Image and Signal Processing, BioMedical Engineering and Informatics (CISP-BMEI)*, pp. 1–5. IEEE, 2022.
- Fontana, M., Zeni, G., and Vantini, S. Conformal prediction: a unified review of theory and new challenges. *Bernoulli*, 29(1):1–23, 2023.
- Fox, M. and Rubin, H. Admissibility of quantile estimates of a single location parameter. *The Annals of Mathematical Statistics*, pp. 1019–1030, 1964.
- Foygel Barber, R., Candes, E. J., Ramdas, A., and Tibshirani, R. J. The limits of distribution-free conditional predictive inference. *Information and Inference: A Journal of the IMA*, 10(2):455–482, 2021.
- Foygel Barber, R., Candes, E. J., Ramdas, A., and Tibshirani, R. J. Conformal prediction beyond exchangeability. *arXiv preprint arXiv:2202.13415*, 2022.
- Fürst, A., Rumetshofer, E., Lehner, J., Tran, V. T., Tang, F., Ramsauer, H., Kreil, D. P., Kopp, M. K., Klambauer, G., Bitto-Nemling, A., and Hochreiter, S. CLOOB: Modern Hopfield Networks with infoLOOB outperform CLIP. In Oh, A. H., Agarwal, A., Belgrave, D., and Cho, K. (eds.), *Advances in Neural Information Processing Systems*, 2022.
- Gal, Y. and Ghahramani, Z. Dropout as a bayesian approximation: Representing model uncertainty in deep learning. In *international conference on machine learning*, pp. 1050–1059. PMLR, 2016.

- Gardner, E. Multiconnected neural network models. *Journal of Physics A*, 20(11):3453–3464, 1987. doi: 10.1088/0305-4470/20/11/046.
- Gibbs, I. and Candes, E. J. Adaptive conformal inference under distribution shift. *Advances in Neural Information Processing Systems*, 34:1660–1672, 2021.
- Gneiting, T. and Katzfuss, M. Probabilistic forecasting. *Annual Review of Statistics and Its Application*, 1(1):125–151, 2014. doi: 10.1146/annurev-statistics-062713-085831.
- Hamilton, J. D. Analysis of time series subject to changes in regime. *Journal of econometrics*, 45(1-2):39–70, 1990.
- Herzen, J., Lässig, F., Piazzetta, S. G., Neuer, T., Tafti, L., Raille, G., Van Pottelbergh, T., Pasięka, M., Skrodzki, A., Huguenin, N., et al. Darts: User-friendly modern machine learning for time series. *Journal of Machine Learning Research*, 23(124):1–6, 2022.
- Hochreiter, S. and Schmidhuber, J. Long short-term memory. *Neural Comput.*, 9(8):1735–1780, 1997.
- Hopfield, J. J. Neural networks and physical systems with emergent collective computational abilities. *Proceedings of the National Academy of Sciences*, 79(8):2554–2558, 1982.
- Hopfield, J. J. Neurons with graded response have collective computational properties like those of two-state neurons. *Proceedings of the National Academy of Sciences*, 81(10):3088–3092, 1984. doi: 10.1073/pnas.81.10.3088.
- Horn, D. and Usher, M. Capacities of multiconnected memory models. *Journal of Physics France*, 49(3):389–395, 1988. doi: 10.1051/jphys:01988004903038900.
- Jensen, V., Bianchi, F. M., and Anfinson, S. N. Ensemble conformalized quantile regression for probabilistic time series forecasting. *arXiv preprint arXiv:2202.08756*, 2022.
- Klotz, D., Kratzert, F., Gauch, M., Keefe Sampson, A., Brandstetter, J., Klambauer, G., Hochreiter, S., and Nearing, G. Uncertainty estimation with deep learning for rainfall–runoff modeling. *Hydrology and Earth System Sciences*, 26(6):1673–1693, 2022. doi: 10.5194/hess-26-1673-2022.
- Kratzert, F., Klotz, D., Shalev, G., Klambauer, G., Hochreiter, S., and Nearing, G. Towards learning universal, regional, and local hydrological behaviors via machine learning applied to large-sample datasets. *Hydrology and Earth System Sciences*, 23(12):5089–5110, 2019. doi: 10.5194/hess-23-5089-2019.
- Kratzert, F., Klotz, D., Hochreiter, S., and Nearing, G. S. A note on leveraging synergy in multiple meteorological data sets with deep learning for rainfall–runoff modeling. *Hydrology and Earth System Sciences*, 25(5):2685–2703, 2021.
- Kratzert, F., Gauch, M., Nearing, G., and Klotz, D. NeuralHydrology — a Python library for deep learning research in hydrology. *Journal of Open Source Software*, 7(71):4050, 2022. doi: 10.21105/joss.04050.
- Krotov, D. and Hopfield, J. J. Dense associative memory for pattern recognition. In Lee, D. D., Sugiyama, M., Luxburg, U. V., Guyon, I., and Garnett, R. (eds.), *Advances in Neural Information Processing Systems*, pp. 1172–1180. Curran Associates, Inc., 2016.
- Krzysztofowicz, R. The case for probabilistic forecasting in hydrology. *Journal of hydrology*, 249(1-4):2–9, 2001.
- Lei, J. and Wasserman, L. A. Distribution-free prediction bands for non-parametric regression. *Journal of the Royal Statistical Society: Series B (Statistical Methodology)*, 76, 2014.
- Loshchilov, I. and Hutter, F. Decoupled weight decay regularization. In *7th International Conference on Learning Representations, ICLR 2019, New Orleans, LA, USA, May 6-9, 2019*. OpenReview.net, 2019.

- Masserano, L., Rangapuram, S. S., Kapoor, S., Nirwan, R. S., Park, Y., and Bohlke-Schneider, M. Adaptive sampling for probabilistic forecasting under distribution shift. In *NeurIPS 2022 Workshop on Distribution Shifts: Connecting Methods and Applications*, 2022.
- Maurer, E. P., Wood, A. W., Adam, J. C., Lettenmaier, D. P., and Nijssen, B. A long-term hydrologically based dataset of land surface fluxes and states for the conterminous United States. *Journal of climate*, 15(22):3237–3251, 2002.
- Newman, A. J., Clark, M. P., Sampson, K., Wood, A., Hay, L. E., Bock, A., Viger, R. J., Blodgett, D., Brekke, L., Arnold, J. R., Hopson, T., and Duan, Q. Development of a large-sample watershed-scale hydrometeorological data set for the contiguous USA: data set characteristics and assessment of regional variability in hydrologic model performance. *Hydrology and Earth System Sciences*, 19(1):209–223, 2015. doi: 10.5194/hess-19-209-2015.
- Newman, A. J., Mizukami, N., Clark, M. P., Wood, A. W., Nijssen, B., and Nearing, G. Benchmarking of a physically based hydrologic model. *Journal of Hydrometeorology*, 18(8):2215–2225, 2017. doi: 10.1175/JHM-D-16-0284.1.
- Oreshkin, B. N., Carпов, D., Chapados, N., and Bengio, Y. N-beats: Neural basis expansion analysis for interpretable time series forecasting. In *International Conference on Learning Representations*, 2020. URL <https://openreview.net/forum?id=r1ecqn4YwB>.
- Paischer, F., Adler, T., Patil, V., Bitto-Nemling, A., Holzleitner, M., Lehner, S., Eghbal-zadeh, H., and Hochreiter, S. History compression via language models in reinforcement learning. In Chaudhuri, K., Jegelka, S., Song, L., Szepesvari, C., Niu, G., and Sabato, S. (eds.), *Proceedings of the 39th International Conference on Machine Learning*, volume 162 of *Proceedings of Machine Learning Research*, pp. 17156–17185. PMLR, 17–23 Jul 2022.
- Papadopoulos, H. and Haralambous, H. Reliable prediction intervals with regression neural networks. *Neural Networks*, 24(8):842–851, 2011.
- Paszke, A., Gross, S., Massa, F., Lerer, A., Bradbury, J., Chanan, G., Killeen, T., Lin, Z., Gimeshain, N., Antiga, L., et al. Pytorch: An imperative style, high-performance deep learning library. *Advances in neural information processing systems*, 32, 2019.
- Pedregosa, F., Varoquaux, G., Gramfort, A., Michel, V., Thirion, B., Grisel, O., Blondel, M., Prettenhofer, P., Weiss, R., Dubourg, V., Vanderplas, J., Passos, A., Cournapeau, D., Brucher, M., Perrot, M., and Duchesnay, E. Scikit-learn: Machine learning in Python. *Journal of Machine Learning Research*, 12:2825–2830, 2011.
- Pinsker, M. S. *Information and information stability of random variables and processes*. Holden-Day, 1964.
- Poyatos, R., Granda, V., Flo, V., Adams, M. A., Adorján, B., Aguadé, D., Aidar, M. P., Allen, S., Alvarado-Barrientos, M. S., Anderson-Teixeira, K. J., et al. Global transpiration data from sap flow measurements: the sapfluxnet database. *Earth system science data*, 13(6):2607–2649, 2021.
- Psaltis, D. and Cheol, H. P. Nonlinear discriminant functions and associative memories. *AIP Conference Proceedings*, 151(1):370–375, 1986. doi: 10.1063/1.36241.
- Quandt, R. E. The estimation of the parameters of a linear regression system obeying two separate regimes. *Journal of the american statistical association*, 53(284):873–880, 1958.
- Ramsauer, H., Schäfl, B., Lehner, J., Seidl, P., Widrich, M., Gruber, L., Holzleitner, M., Pavlović, M., Sandve, G. K., Greiff, V., Kreil, D., Kopp, M., Klambauer, G., Brandstetter, J., and Hochreiter, S. Hopfield networks is all you need. In *9th International Conference on Learning Representations (ICLR)*, 2021.
- Salinas, D., Flunkert, V., Gasthaus, J., and Januschowski, T. Deepar: Probabilistic forecasting with autoregressive recurrent networks. *International Journal of Forecasting*, 36(3):1181–1191, 2020.
- Sanchez-Fernandez, A., Rumetshofer, E., Hochreiter, S., and Klambauer, G. CLOOME: contrastive learning unlocks bioimaging databases for queries with chemical structures. In *NeurIPS 2022 Women in Machine Learning Workshop*, 2022.

- Sanquer, M., Chatelain, F., El-Guedri, M., and Martin, N. A smooth transition model for multiple-regime time series. *IEEE transactions on signal processing*, 61(7):1835–1847, 2012.
- Schäfl, B., Gruber, L., Bitto-Nemling, A., and Hochreiter, S. Hopular: Modern Hopfield Networks for tabular data. *arXiv preprint arXiv:2206.00664*, 2022.
- Sengupta, M., Xie, Y., Lopez, A., Habte, A., Maclaurin, G., and Shelby, J. The national solar radiation data base (NSRDB). *Renewable and sustainable energy reviews*, 89:51–60, 2018.
- Smyl, S. A hybrid method of exponential smoothing and recurrent neural networks for time series forecasting. *International Journal of Forecasting*, 36(1):75–85, 2020.
- Stankevičiūtė, K., M Alaa, A., and van der Schaar, M. Conformal time-series forecasting. *Advances in Neural Information Processing Systems*, 34:6216–6228, 2021.
- Sun, S. and Yu, R. Copula conformal prediction for multi-step time series forecasting. *ArXiv*, abs/2212.03281, 2022.
- Sun, X., Kim, S., and Choi, J.-I. Recurrent neural network-induced gaussian process. *Neurocomputing*, 509:75–84, 2022.
- Tagasovska, N. and Lopez-Paz, D. Single-model uncertainties for deep learning. *Advances in Neural Information Processing Systems*, 32, 2019.
- Tajeuna, E. G., Bouguessa, M., and Wang, S. Modeling regime shifts in multiple time series. *arXiv preprint arXiv:2109.09692*, 2021.
- Teng, J., Wen, C., Zhang, D., Bengio, Y., Gao, Y., and Yuan, Y. Predictive inference with feature conformal prediction. *arXiv preprint arXiv:2210.00173*, 2022.
- Thornton, P. E., Running, S. W., White, M. A., et al. Generating surfaces of daily meteorological variables over large regions of complex terrain. *Journal of hydrology*, 190(3-4):214–251, 1997.
- Tibshirani, R. J., Foygel Barber, R., Candès, E. J., and Ramdas, A. Conformal prediction under covariate shift. *Advances in Neural Information Processing Systems*, 32, 2019.
- Tocaceli, P., Nouredinov, I., and Gammerman, A. Conformal prediction of biological activity of chemical compounds. *Annals of Mathematics and Artificial Intelligence*, 81(1):105–123, 2017.
- Vaswani, A., Shazeer, N., Parmar, N., Uszkoreit, J., Jones, L., Gomez, A. N., Kaiser, L., and Polosukhin, I. Attention is all you need. In Guyon, I., Luxburg, U. V., Bengio, S., Wallach, H., Fergus, R., Vishwanathan, S., and Garnett, R. (eds.), *Advances in Neural Information Processing Systems 30*, pp. 5998–6008. Curran Associates, Inc., 2017.
- Vovk, V. Conditional validity of inductive conformal predictors. In *Asian conference on machine learning*, pp. 475–490. PMLR, 2012.
- Vovk, V., Gammerman, A., and Saunders, C. Machine-learning applications of algorithmic randomness. In Bratko, I. and Dzeroski, S. (eds.), *Proceedings of the Sixteenth International Conference on Machine Learning (ICML 1999), Bled, Slovenia, June 27 - 30, 1999*, pp. 444–453. Morgan Kaufmann, 1999.
- Vovk, V., Gammerman, A., and Shafer, G. *Algorithmic learning in a random world*. Springer Science & Business Media, 2005.
- Widrich, M., Schäfl, B., Pavlović, M., Ramsauer, H., Gruber, L., Holzleitner, M., Brandstetter, J., Sandve, G. K., Greiff, V., Hochreiter, S., and Klambauer, G. Modern Hopfield Networks and attention for immune repertoire classification. In *Advances in Neural Information Processing Systems*. Curran Associates, Inc., 2020.
- Winkler, R. L. A decision-theoretic approach to interval estimation. *Journal of the American Statistical Association*, 67(337):187–191, 1972.

- Xia, Y., Mitchell, K., Ek, M., Sheffield, J., Cosgrove, B., Wood, E., Luo, L., Alonge, C., Wei, H., Meng, J., et al. Continental-scale water and energy flux analysis and validation for the North American Land Data Assimilation System project phase 2 (NLDAS-2): 1. intercomparison and application of model products. *Journal of Geophysical Research: Atmospheres*, 117(D3), 2012.
- Xu, C. and Xie, Y. Conformal prediction for time series. *arXiv preprint arXiv:2010.09107*, 2022a.
- Xu, C. and Xie, Y. Sequential predictive conformal inference for time series. *arXiv preprint arXiv:2212.03463*, 2022b.
- Xu, Y., Yu, W., Ghamisi, P., Kopp, M., and Hochreiter, S. Txt2Img-MHN: Remote sensing image generation from text using Modern Hopfield Networks. *arXiv preprint arXiv:2208.04441*, 2022.
- Zaffran, M., Féron, O., Goude, Y., Josse, J., and Dieuleveut, A. Adaptive conformal predictions for time series. In *International Conference on Machine Learning*, pp. 25834–25866. PMLR, 2022.
- Zhang, S., Guo, B., Dong, A., He, J., Xu, Z., and Chen, S. X. Cautionary tales on air-quality improvement in Beijing. *Proceedings of the Royal Society A: Mathematical, Physical and Engineering Sciences*, 473(2205):20170457, 2017.
- Zhu, L. and Laptev, N. Deep and confident prediction for time series at Uber. In *2017 IEEE International Conference on Data Mining Workshops (ICDMW)*, pp. 103–110. IEEE, 2017.
- Zhu, X., Huang, L., Lee, E. H., Ibrahim, C. A., and Bindel, D. Bayesian transformed gaussian processes. *Transactions on Machine Learning Research*, 2023.

A Extended Experimental Setup & Results

A.1 Hyperparameter Search

We conducted an individual hyperparameter grid search for each predictor–dataset combination. For methods that require calibration data (HopCPT, AdaptiveCI, NexCP), each calibration set was split in half: One part served as actual calibration data while the other half was used for validation.⁴ As EnbPI requires only the k past points, we used the full calibration set minus these k points for validation, so that it could fully exploit the available data. Table 2 shows all sets of hyperparameters used for the search.

Table 2: Parameters used in the hyperparameter search of the uncertainty models

Method	Parameter	Value
HopCPT	Learning Rate	0.01, 0.001
	Dropout	0, 0.25, 0.5
	Time Encode	yes/no
AdaptiveCI	Mode	simple, momentum
	γ	0.002, 0.005, 0.01, 0.02
EnbPI	Window Length	200, 150, 125, 100, 75, 50, 25, 10
NexCP	ρ	0.999, 0.995, 0.993, 0.99, 0.98, 0.95, 0.90
kNN	k-Top Share	0.025, 0.05, 0.10, 0.15, 0.20, 0.25, 0.30, 0.35
MCD	Learning Rate	0.005, 0.001, 0.0001
	Dropout	0.1, 0.25, 0.5
	Batch Size	512, 256
	Hidden Size	64, 128, 256
Gaus	Learning Rate	0.005, 0.001, 0.0001
	Dropout	0, 0.1, 0.25
	Batch Size	512, 256
	Hidden Size	64, 128, 256
MDN	Learning Rate	0.005, 0.001, 0.0001
	Dropout	0, 0.1, 0.25
	Batch Size	512, 256
	Hidden Size	64, 128, 256
	# Components	3, 5, 7

Model selection. Model selection was done uniformly for all algorithms: As a first step, all models with a negative Δ Cov on the validation set were excluded. From the remaining models, the model with the smallest PI-Width was selected. In cases where no model achieved non-negative Δ Cov, the model with the highest Δ Cov was selected.

HopCPT. HopCPT was trained for 3,000 epochs in each experiment. We chose this number to make sure that the loss and model selection metric curves are already converged. Throughout training, we validated every 5 epochs and selected the model that best fulfilled the model selection criteria described above. AdamW (Loshchilov & Hutter, 2019) with standard parameters ($\beta_1 = 0.9$, $\beta_2 = 0.999$, $\delta = 0.01$) was used as optimizer. The learning rate was part of the hyperparameter search. Depending on the dataset size, the batch size was set to 2 or 4, where a batch size of n would mean that the full training part of the calibration set of n time series is used.

⁴Note that this is only the case in the hyperparameter search. In the evaluation, the full calibration set was used for calibration.

SPCI. The computational demand of SPCI did not allow to conduct a full hyperparameter search for the window length parameter (see more in Section A.2). Since SPCI applies a random forest on the window, one can assume that it is capable to find the relevant parts of the window. On top of that, a longer window has less risk than a window that is too short and (potentially) cuts off relevant information. Hence, we set the window length to 100 for all experiments, which corresponds to the longest setting in the original paper. To check our reasoning, we evaluated the performance of SPCI with window length 25 on all but the largest two datasets (Table 4 and Table 5). We found hardly any differences except for the smallest datasets Solar (3M). In that case we reason that the result is due to the limited calibration data in this setting.

MCD/MDN/Gauss. In Appendix A.3 we compare HopCPT to non-CP architectures that can provide prediction interval estimates. Specifically, we use Monte Carlo Dropout (MCD; Gal & Ghahramani, 2016), a Mixture Density Network (MDN; Bishop, 1994), and a Gauss model (i.e., an MDN with a single Gaussian density). An LSTM serves as backbone for all models. Therefore, there is no distinction between the predictor model and the uncertainty model. To allow for a fair comparison to CP approaches, the models are trained on both the predictor training data and the calibration data combined. None of these approaches are CP methods, and MCD was specifically devised to estimate only epistemic uncertainty. Nevertheless, we consider these methods as useful comparisons, since they are widely used for uncertainty quantification. The models were trained for 150 epochs with AdamW (Loshchilov & Hutter, 2019) (using its standard parameters: $\beta_1 = 0.9$, $\beta_2 = 0.999$, $\delta = 0.001$). We chose this number to ensure that the loss and model selection metrics already converged. Throughout the training, we validated after every epoch and selected the model that best fulfilled the model selection criteria described above. The learning rate was part of the hyperparameter search.

Global LSTM. We conducted an individual hyperparameter tuning of the global LSTM prediction model for each dataset. Table 3 shows the hyperparameters used for the grid search. Similar to the LSTM uncertainty models, we trained for 150 epochs with an AdamW optimizer (Loshchilov & Hutter, 2019) and validated after each epoch. We optimized for the mean squared error and selected the model with the smallest validation mean squared error.

Table 3: Parameters used in the hyperparameter search of the global LSTM prediction model.

Parameter	Value
Learning Rate	0.005, 0.001, 0.0001
Dropout	0, 0.1, 0.25
Batch Size	512, 256
Hidden Size	64, 128, 256

A.2 SPCI Retraining

As our results show, SPCI is very competitive (see, for example, Section 3.2). Xu & Xie (2022b) did, however, design SPCI so that its random forest regressor is retrained after each prediction step. This design choice is computationally prohibitive for larger datasets. To nevertheless allow a comparison against SPCI on the larger datasets, we modified the algorithm so that the retraining is skipped. Experiments on the smallest dataset (Table 6) show only small performance decrease with the modified algorithm. One limitation of the adapted algorithm is, however, that a strong shift in the error distribution(s) would potentially require a retraining on the new distribution. A viable proxy to detect such a change in our setting is the coverage performance of standard CP. The reason for this is that standard CP predictions are solely based on the calibration data and can thus not account for shifts. In the experiments (Section 3 and Appendix A.3), standard CP achieves good coverage with only one exception (see Section 3). Hence, we decided to include SPCI (in the modified version) to enable a comparison to it on larger datasets.

Table 4: Performance of SPCI with an input window of length 100 and length 25 on the solar datasets. The differences in performance are small compared to the differences across methods (Section 3.2). The error term represents the standard deviation over repeated runs.

Data	FC	Window	100	25
Solar IY	Forest	Δ Cov	$0.045^{\pm 0.000}$	$0.047^{\pm 0.000}$
		PI-Width	$97.2^{\pm 0.1}$	$97.8^{\pm 0.3}$
		Winkler	$1.26^{\pm 0.00}$	$1.25^{\pm 0.00}$
	LGBM	Δ Cov	$0.045^{\pm 0.000}$	$0.047^{\pm 0.000}$
		PI-Width	$96.6^{\pm 0.2}$	$97.6^{\pm 0.1}$
		Winkler	$1.26^{\pm 0.00}$	$1.26^{\pm 0.00}$
	Ridge	Δ Cov	$0.031^{\pm 0.000}$	$0.030^{\pm 0.000}$
		PI-Width	$112.9^{\pm 0.2}$	$113.7^{\pm 0.1}$
		Winkler	$1.40^{\pm 0.00}$	$1.42^{\pm 0.00}$
LSTM	Δ Cov	$0.018^{\pm 0.000}$	$0.018^{\pm 0.000}$	
	PI-Width	$22.5^{\pm 0.0}$	$22.2^{\pm 0.0}$	
	Winkler	$0.41^{\pm 0.00}$	$0.40^{\pm 0.00}$	
Solar Small	Forest	Δ Cov	$-0.064^{\pm 0.002}$	$-0.024^{\pm 0.000}$
		PI-Width	$38.8^{\pm 0.4}$	$43.2^{\pm 0.2}$
		Winkler	$1.82^{\pm 0.01}$	$1.53^{\pm 0.00}$
	LGBM	Δ Cov	$-0.052^{\pm 0.002}$	$-0.027^{\pm 0.001}$
		PI-Width	$37.4^{\pm 0.2}$	$43.3^{\pm 0.1}$
		Winkler	$1.84^{\pm 0.01}$	$1.63^{\pm 0.00}$
	Ridge	Δ Cov	$-0.055^{\pm 0.002}$	$-0.057^{\pm 0.001}$
		PI-Width	$51.9^{\pm 0.2}$	$52.8^{\pm 0.2}$
		Winkler	$1.91^{\pm 0.02}$	$1.83^{\pm 0.00}$

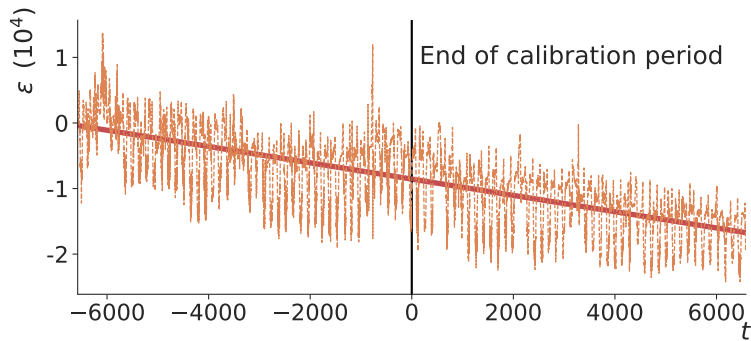


Figure 4: Time series of the prediction error ϵ for the ridge regression model on the Sap flow dataset. The time series spans the calibration ($t < 0$) and test ($t \geq 0$) data. The red line (fitted by the least squares method) shows a strong trend in the error distribution.

Table 5: Performance of SPCI with an input window of length 100 and length 25 on the different non-solar datasets. The differences in performance are small compared to the differences across methods (Section 3.2). The error term represents the standard deviation over repeated runs.

Data	FC	Window	100	25
Air 10 PM	Forest	Δ Cov	$0.008^{\pm 0.000}$	$0.008^{\pm 0.000}$
		PI-Width	$118.5^{\pm 0.0}$	$118.5^{\pm 0.1}$
		Winkler	$2.23^{\pm 0.00}$	$2.23^{\pm 0.00}$
	LGBM	Δ Cov	$0.024^{\pm 0.000}$	$0.023^{\pm 0.000}$
		PI-Width	$113.2^{\pm 0.2}$	$113.2^{\pm 0.1}$
		Winkler	$1.94^{\pm 0.00}$	$1.94^{\pm 0.00}$
	Ridge	Δ Cov	$0.024^{\pm 0.000}$	$0.024^{\pm 0.000}$
		PI-Width	$93.9^{\pm 0.0}$	$93.8^{\pm 0.0}$
		Winkler	$1.52^{\pm 0.00}$	$1.52^{\pm 0.00}$
	LSTM	Δ Cov	$0.010^{\pm 0.000}$	$0.010^{\pm 0.000}$
		PI-Width	$62.3^{\pm 0.1}$	$62.3^{\pm 0.0}$
		Winkler	$1.21^{\pm 0.00}$	$1.21^{\pm 0.00}$
Air 25 PM	Forest	Δ Cov	$-0.009^{\pm 0.000}$	$-0.009^{\pm 0.000}$
		PI-Width	$81.5^{\pm 0.0}$	$81.4^{\pm 0.0}$
		Winkler	$2.02^{\pm 0.00}$	$2.02^{\pm 0.00}$
	LGBM	Δ Cov	$0.002^{\pm 0.001}$	$0.001^{\pm 0.000}$
		PI-Width	$73.3^{\pm 0.0}$	$73.3^{\pm 0.0}$
		Winkler	$1.84^{\pm 0.00}$	$1.83^{\pm 0.00}$
	Ridge	Δ Cov	$0.010^{\pm 0.000}$	$0.010^{\pm 0.000}$
		PI-Width	$65.5^{\pm 0.0}$	$65.4^{\pm 0.1}$
		Winkler	$1.40^{\pm 0.00}$	$1.40^{\pm 0.00}$
	LSTM	Δ Cov	$-0.017^{\pm 0.000}$	$-0.017^{\pm 0.000}$
		PI-Width	$32.4^{\pm 0.0}$	$32.3^{\pm 0.0}$
		Winkler	$0.93^{\pm 0.00}$	$0.92^{\pm 0.00}$
Sap flow	Forest	Δ Cov	$0.007^{\pm 0.000}$	$0.007^{\pm 0.000}$
		PI-Width	$1743.1^{\pm 1.4}$	$1742.7^{\pm 1.2}$
		Winkler	$0.59^{\pm 0.00}$	$0.59^{\pm 0.00}$
	LGBM	Δ Cov	$0.003^{\pm 0.000}$	$0.003^{\pm 0.000}$
		PI-Width	$1581.9^{\pm 0.7}$	$1583.6^{\pm 1.3}$
		Winkler	$0.49^{\pm 0.00}$	$0.49^{\pm 0.00}$
	Ridge	Δ Cov	$-0.241^{\pm 0.000}$	$-0.242^{\pm 0.000}$
		PI-Width	$2061.5^{\pm 1.4}$	$2066.8^{\pm 1.2}$
		Winkler	$2.52^{\pm 0.00}$	$2.52^{\pm 0.00}$
	LSTM	Δ Cov	$0.004^{\pm 0.000}$	$0.006^{\pm 0.000}$
		PI-Width	$628.6^{\pm 0.8}$	$631.9^{\pm 0.2}$
		Winkler	$0.24^{\pm 0.00}$	$0.24^{\pm 0.00}$

Table 6: Performance of the original SPCI algorithm (Retrain) and the modified version (No Retrain) on the Solar (3M) dataset. Performance in terms of the evaluation metrics is similar compared to the differences between methods (Section 3.2). The computational demand of the modified version is considerably lower. The error term represents the standard deviation over repeated runs.

FC	α	UC	No Retrain	Retrain
Forest	0.05	Δ Cov	$-0.074^{\pm 0.001}$	$-0.049^{\pm 0.001}$
		PI-Width	$58.0^{\pm 0.2}$	$62.4^{\pm 0.0}$
		Winkler	$2.62^{\pm 0.03}$	$2.28^{\pm 0.01}$
	0.10	Δ Cov	$-0.064^{\pm 0.002}$	$-0.045^{\pm 0.003}$
		PI-Width	$38.8^{\pm 0.4}$	$41.6^{\pm 0.0}$
		Winkler	$1.82^{\pm 0.01}$	$1.67^{\pm 0.00}$
	0.15	Δ Cov	$-0.050^{\pm 0.002}$	$-0.038^{\pm 0.003}$
		PI-Width	$26.8^{\pm 0.2}$	$28.9^{\pm 0.0}$
		Winkler	$1.44^{\pm 0.02}$	$1.35^{\pm 0.00}$
LGBM	0.05	Δ Cov	$-0.062^{\pm 0.001}$	$-0.061^{\pm 0.001}$
		PI-Width	$56.1^{\pm 0.4}$	$58.2^{\pm 0.0}$
		Winkler	$2.65^{\pm 0.03}$	$2.51^{\pm 0.01}$
	0.10	Δ Cov	$-0.052^{\pm 0.002}$	$-0.049^{\pm 0.001}$
		PI-Width	$37.4^{\pm 0.2}$	$39.8^{\pm 0.0}$
		Winkler	$1.84^{\pm 0.01}$	$1.78^{\pm 0.01}$
	0.15	Δ Cov	$-0.042^{\pm 0.001}$	$-0.037^{\pm 0.001}$
		PI-Width	$26.9^{\pm 0.3}$	$28.3^{\pm 0.0}$
		Winkler	$1.47^{\pm 0.00}$	$1.42^{\pm 0.00}$
Ridge	0.05	Δ Cov	$-0.063^{\pm 0.001}$	$-0.056^{\pm 0.002}$
		PI-Width	$67.3^{\pm 0.2}$	$68.7^{\pm 0.0}$
		Winkler	$2.47^{\pm 0.01}$	$2.25^{\pm 0.01}$
	0.10	Δ Cov	$-0.055^{\pm 0.002}$	$-0.048^{\pm 0.001}$
		PI-Width	$51.9^{\pm 0.2}$	$54.2^{\pm 0.0}$
		Winkler	$1.91^{\pm 0.02}$	$1.77^{\pm 0.01}$
	0.15	Δ Cov	$-0.039^{\pm 0.003}$	$-0.036^{\pm 0.000}$
		PI-Width	$43.1^{\pm 0.3}$	$45.0^{\pm 0.0}$
		Winkler	$1.59^{\pm 0.00}$	$1.50^{\pm 0.00}$

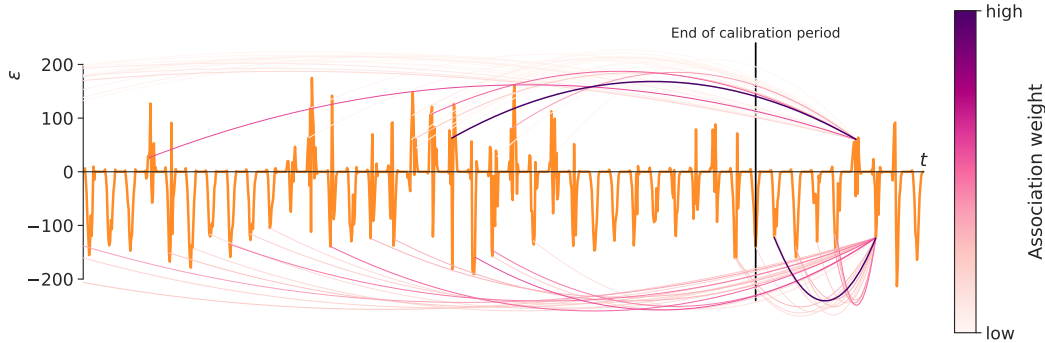


Figure 5: Visualization of the 30 highest association weights that the Hopfield network places on previous time steps. HopCPT retrieves similar error values when predicting at a time of high error, and it retrieves similar, previous small errors when predicting at a time step with small error.

A.3 Additional Results

Tables 17–23 show the results for miscoverage levels $\alpha \in \{0.05, 0.10, 0.15\}$ for all evaluated combinations of datasets and predictors. Results for individual time series of the datasets are uploaded to the code repository (Appendix J).

CMAL. For the Streamflow dataset, we additionally compare to CMAL, which is the state-of-the-art non-CP uncertainty estimation technique in the respective domain (Klotz et al., 2022). CMAL is a mixture density network (Bishop, 1994) based on an LSTM that predicts the parameters of asymmetric Laplacian distributions. As our experiments use the same dataset, we adopt the hyperparameters from Klotz et al. (2022) but lower the learning rate to 0.0001 because we train CMAL on more training samples (18 years, i.e., the training and calibration period combined, which allows for a fair comparison against the CP methods). Despite the fact that CMAL is not based on the CP paradigm, it achieves good coverage results, however, at the cost of wide prediction intervals. We argue that the Winkler score is low because CMAL considers all (and therefore also uncovered) samples during the optimization while CP methods do not consider them at all — therefore, the distance of these points to the interval might be smaller (see Table 23).

Error trend. Figure 4 shows the prediction errors of the ridge regression model on the Sap flow dataset. The errors exhibit a strong trend and shift towards a negative expectation value.

Association weights. Figure 5 investigates the association patterns of HopCPT and shows its capabilities to focus on time steps from similar error regimes. The depicted time step in a regime with negative errors retrieves time steps with primarily negative errors and, likewise, the time step in a regime with positive errors retrieves time steps with primarily positive errors of the same magnitude.

Non-CP methods We also compare HopCPT to non-CP methods to evaluate its performance within the broader field of uncertainty estimation for time series. Specifically, we compare against a Monte Carlo Dropout (MCD); a Mixture Density Network (MDN), and a Gauss model (i.e., an MDN with a single Gaussian component), with an LSTM backbone (see Appendix A.1 for more details about the models and their hyperparameters). This comparison shows that, although the non-CP methods often lead to very narrow prediction intervals, they fail to provide approximate coverage on most experiments (Table 7).

A.4 Local Coverage

Standard CP only provides marginal coverage guarantees and a constant prediction interval width (Vovk et al., 2005). In time series prediction tasks, this can lead to bad local coverage (Lei & Wasserman, 2014). To evaluate whether the coverage approximately holds also locally, we evaluated ΔCov on windows of size k . To avoid compensation of negative ΔCov in some windows by other windows with positive ΔCov , we upper-bounded each window’s ΔCov by zero before averaging over the bounded coverage gaps — i.e., we calculated $\frac{1}{W} \sum_{w=1}^W -\Delta \text{Cov}_w^{\top 0}$, with

$$\Delta \text{Cov}_w^{\top 0} = \begin{cases} \Delta \text{Cov}_w & \text{if } \Delta \text{Cov}_w \leq 0, \\ 0 & \text{else,} \end{cases} \quad (10)$$

where ΔCov_w is the ΔCov within window w .

Table 8 shows the results of this evaluation for window sizes $k \in \{10, 20, 50\}$ and miscoverage level $\alpha = 0.1$. Depending on the dataset, most often either HopCPT or SPCI perform best. The overall rankings are only partly similar to the evaluation of the marginal coverage (Table 1 and Appendix A.3). Especially standard CP, which achieves competitive results in marginal coverage, falls short in this comparison. Only for Solar (3M), where the approach achieves a high marginal ΔCov , it preserves the local coverage best. Note that this comes with the drawback of very wide prediction intervals, i.e., bad efficiency. Overall, the results show that HopCPT and other time series CP methods improve the local coverage in non-exchangeable time series settings, compared to standard CP.

A.5 Negative Results

We also tested training with more involved training procedures than directly using the mean squared error. However, based on our empirical findings, the vanilla method with mean squared error outperforms more complex approaches. In the following, we briefly describe those additional configurations (so that potential future research can avoid these paths):

- **Pinball Loss.** We tried to train the MHN with a pinball loss (the original use seems to stem from Fox & Rubin, 1964, we are however not aware of the naming origin) in many different variations (see points that follow), but consistently got worse results than with the mean squared error.
 - Inspired by the ideas lined out by Tagasovska & Lopez-Paz (2019) we tried to use the miscoverage level as an additional input to the network, while also parameterizing the loss with it.
 - We tried to use the pinball loss to predict multiple miscoverage values at the same time to get a more informed representation of the distribution we want to approximate.
- **Softmax Probabilities.** We tried to use the softmax output of the MHN to directly estimate probabilities and use a maximum likelihood procedure. This did train, but it did not produce good results.

A.6 Computational Resources

We used different hardware setups in our experiments, however, most of them were executed on a machine with an Nvidia P100 GPU and a Xeon E5-2698 CPU. The runtime differs greatly between different dataset sizes. We report the approximate run times for a single experiment (i.e., one seed, all evaluated coverage levels, not including training the prediction model $\hat{\mu}$):

1. **HopCPT:** Solar (3Y) 5h, Solar (1Y) 1h, Solar (3M) 7min, Air Quality (10PM) 3h, Air Quality (25PM) 3h, Sap flow 2.5h, Streamflow 12–20h
2. **SPCI:** (adapted): Solar (3Y) 5–10 days, Solar (1Y) 10–30h, Solar (3M) 45min, Air Quality (10PM) 13–30h, Air Quality (25PM) 13–30h, Sap flow 20–50h, Streamflow 12–17 days
3. **EnbPI:** all datasets under 6h
4. **NexCP:** all datasets under 45min
5. **AdaptiveCI:** all datasets under 45min
6. **Standard CP:** all datasets under 45min

Table 7: Performance of the best two CP methods (HopCPT and SPCI) and state-of-the-art non-CP methods for the different datasets and levels of α . All approaches build upon an LSTM model. Bold numbers correspond to the best result for the respective metric in the experiment (PI-Width and Winkler score), given that $\Delta\text{Cov} \geq -0.25\alpha$, i.e., the specific algorithm reached at least approximate coverage (the result is grayed out otherwise). The error term represents the standard deviation over repeated runs with different seeds (results without an error term are from deterministic models).

			HopCPT	SPCI	MCD	Gauss	MDN
		α					
Solar 3Y	0.05	ΔCov	-0.003 \pm 0.005	0.004 \pm 0.000	-0.058 \pm 0.004	-0.331 \pm 0.243	-0.005 \pm 0.013
		PI-Width	22.7 \pm 0.8	47.7 \pm 0.0	17.5 \pm 0.1	25.9 \pm 4.1	16.2 \pm 1.0
		Winkler	0.38 \pm 0.01	0.87 \pm 0.00	0.75 \pm 0.01	0.46 \pm 0.10	0.33 \pm 0.06
	0.10	ΔCov	0.001 \pm 0.006	0.014 \pm 0.000	-0.030 \pm 0.006	-0.310 \pm 0.238	-0.013 \pm 0.047
		PI-Width	17.9 \pm 0.6	27.8 \pm 0.0	14.8 \pm 0.1	21.8 \pm 3.5	13.2 \pm 0.8
		Winkler	0.30 \pm 0.01	0.62 \pm 0.00	0.49 \pm 0.00	0.37 \pm 0.06	0.26 \pm 0.03
	0.15	ΔCov	0.002 \pm 0.007	0.024 \pm 0.000	0.001 \pm 0.007	-0.320 \pm 0.166	-0.053 \pm 0.141
		PI-Width	15.0 \pm 0.4	18.1 \pm 0.0	12.9 \pm 0.1	19.1 \pm 3.0	11.4 \pm 0.8
		Winkler	0.26 \pm 0.00	0.48 \pm 0.00	0.38 \pm 0.00	0.32 \pm 0.04	0.23 \pm 0.02
Solar 1Y	0.05	ΔCov	0.019 \pm 0.003	0.006 \pm 0.000	-0.041 \pm 0.004	-0.109 \pm 0.191	-0.055 \pm 0.104
		PI-Width	21.4 \pm 0.7	37.0 \pm 0.0	20.5 \pm 0.3	14.6 \pm 0.8	13.2 \pm 1.4
		Winkler	0.27 \pm 0.01	0.58 \pm 0.00	0.58 \pm 0.01	0.22 \pm 0.01	0.20 \pm 0.03
	0.10	ΔCov	0.028 \pm 0.010	0.018 \pm 0.000	-0.011 \pm 0.005	-0.134 \pm 0.253	-0.130 \pm 0.182
		PI-Width	16.0 \pm 0.6	22.5 \pm 0.0	17.3 \pm 0.2	12.3 \pm 0.7	10.8 \pm 1.2
		Winkler	0.22 \pm 0.01	0.41 \pm 0.00	0.40 \pm 0.01	0.18 \pm 0.01	0.17 \pm 0.02
	0.15	ΔCov	0.029 \pm 0.017	0.032 \pm 0.000	0.022 \pm 0.006	-0.148 \pm 0.236	-0.185 \pm 0.224
		PI-Width	13.1 \pm 0.5	15.3 \pm 0.0	15.2 \pm 0.2	10.8 \pm 0.6	9.3 \pm 1.1
		Winkler	0.19 \pm 0.00	0.32 \pm 0.00	0.32 \pm 0.00	0.16 \pm 0.01	0.15 \pm 0.02
Air 10 PM	0.05	ΔCov	-0.001 \pm 0.001	0.003 \pm 0.000	-0.202 \pm 0.008	-0.191 \pm 0.024	-0.218 \pm 0.115
		PI-Width	90.7 \pm 1.9	86.1 \pm 0.0	42.3 \pm 0.8	45.8 \pm 2.2	43.9 \pm 9.5
		Winkler	1.83 \pm 0.03	1.63 \pm 0.00	2.36 \pm 0.03	2.08 \pm 0.12	2.22 \pm 0.59
	0.10	ΔCov	-0.002 \pm 0.005	0.010 \pm 0.000	-0.201 \pm 0.009	-0.211 \pm 0.026	-0.243 \pm 0.122
		PI-Width	62.7 \pm 1.5	62.2 \pm 0.0	35.7 \pm 0.7	38.6 \pm 1.9	35.3 \pm 7.3
		Winkler	1.33 \pm 0.01	1.21 \pm 0.00	1.49 \pm 0.01	1.42 \pm 0.06	1.48 \pm 0.30
	0.15	ΔCov	-0.002 \pm 0.010	0.017 \pm 0.000	-0.192 \pm 0.009	-0.218 \pm 0.027	-0.252 \pm 0.122
		PI-Width	49.4 \pm 1.7	50.2 \pm 0.0	31.4 \pm 0.6	33.8 \pm 1.7	30.2 \pm 6.0
		Winkler	1.09 \pm 0.01	1.01 \pm 0.00	1.16 \pm 0.01	1.15 \pm 0.04	1.17 \pm 0.20
Air 25 PM	0.05	ΔCov	0.005 \pm 0.005	-0.015 \pm 0.000	-0.100 \pm 0.022	-0.227 \pm 0.018	-0.209 \pm 0.119
		PI-Width	57.1 \pm 5.6	44.9 \pm 0.0	31.7 \pm 3.5	27.1 \pm 1.4	26.9 \pm 6.1
		Winkler	1.19 \pm 0.08	1.29 \pm 0.00	1.41 \pm 0.05	1.58 \pm 0.08	1.57 \pm 0.47
	0.10	ΔCov	0.007 \pm 0.008	-0.017 \pm 0.000	-0.095 \pm 0.027	-0.247 \pm 0.020	-0.234 \pm 0.129
		PI-Width	40.7 \pm 4.3	32.4 \pm 0.0	26.6 \pm 3.0	22.8 \pm 1.2	21.6 \pm 4.9
		Winkler	0.88 \pm 0.05	0.93 \pm 0.00	0.95 \pm 0.03	1.06 \pm 0.04	1.05 \pm 0.24
	0.15	ΔCov	0.005 \pm 0.011	-0.016 \pm 0.000	-0.086 \pm 0.030	-0.253 \pm 0.020	-0.243 \pm 0.131
		PI-Width	32.5 \pm 3.7	26.1 \pm 0.0	23.2 \pm 2.6	20.0 \pm 1.0	18.4 \pm 4.2
		Winkler	0.74 \pm 0.04	0.76 \pm 0.00	0.76 \pm 0.02	0.85 \pm 0.02	0.84 \pm 0.16
Sap flow	0.05	ΔCov	0.001 \pm 0.002	0.000 \pm 0.000	-0.150 \pm 0.007	-0.072 \pm 0.018	-0.059 \pm 0.035
		PI-Width	783.5 \pm 9.2	897.7 \pm 0.9	421.6 \pm 5.2	494.7 \pm 26.0	494.6 \pm 41.2
		Winkler	0.25 \pm 0.01	0.33 \pm 0.00	0.49 \pm 0.01	0.29 \pm 0.02	0.27 \pm 0.06
	0.10	ΔCov	0.004 \pm 0.004	0.004 \pm 0.000	-0.139 \pm 0.007	-0.067 \pm 0.022	-0.067 \pm 0.037
		PI-Width	594.3 \pm 7.7	628.2 \pm 0.9	355.2 \pm 4.3	416.5 \pm 21.9	391.7 \pm 31.4
		Winkler	0.19 \pm 0.01	0.24 \pm 0.00	0.30 \pm 0.01	0.20 \pm 0.01	0.19 \pm 0.03
	0.15	ΔCov	0.005 \pm 0.005	0.006 \pm 0.000	-0.122 \pm 0.007	-0.059 \pm 0.024	-0.068 \pm 0.039
		PI-Width	489.9 \pm 7.0	493.2 \pm 0.5	311.4 \pm 3.8	364.9 \pm 19.2	331.5 \pm 25.8
		Winkler	0.17 \pm 0.01	0.20 \pm 0.00	0.23 \pm 0.01	0.17 \pm 0.01	0.16 \pm 0.02

Table 8: Negative average of zero-upper-bounded Δ Cov of rolling windows with miscoverage level $\alpha = 0.1$. We evaluate each dataset–predictor combination at the windows sizes $k \in \{10, 20, 50\}$.

Data	FC	k	HopCPT	SPCI	EnbPI	NexCP	CP
Solar 3Y	Forest	10	.030	.040	.081	.059	.059
		20	.020	.022	.055	.034	.040
		50	.012	.016	.042	.021	.032
	LGBM	10	.051	.040	.076	.059	.058
		20	.040	.022	.052	.035	.039
		50	.031	.015	.038	.022	.031
	Ridge	10	.023	.049	.099	.055	.056
		20	.014	.035	.083	.039	.040
		50	.007	.028	.075	.027	.030
Solar 1Y	Forest	10	.023	.023	.070	.055	.019
		20	.015	.012	.043	.031	.010
		50	.010	.008	.031	.017	.005
	LGBM	10	.059	.023	.071	.056	.018
		20	.049	.012	.046	.032	.010
		50	.041	.007	.033	.018	.005
	Ridge	10	.063	.030	.070	.055	.066
		20	.053	.021	.055	.038	.052
		50	.045	.016	.043	.027	.045
Solar Small	Forest	10	.045	.108	.074	.075	.083
		20	.026	.074	.046	.045	.055
		50	.015	.067	.034	.030	.042
	LGBM	10	.048	.093	.074	.074	.078
		20	.032	.061	.044	.044	.048
		50	.020	.051	.030	.029	.035
	Ridge	10	.051	.100	.065	.058	.064
		20	.039	.073	.049	.039	.045
		50	.032	.066	.041	.033	.038
Air 10 PM	Forest	10	.033	.049	.124	.075	.106
		20	.025	.042	.114	.067	.100
		50	.018	.035	.099	.053	.089
	LGBM	10	.038	.037	.115	.074	.100
		20	.030	.030	.104	.065	.093
		50	.021	.023	.089	.052	.083
	Ridge	10	.041	.035	.099	.068	.064
		20	.032	.028	.089	.059	.057
		50	.024	.020	.074	.045	.048
Air 25 PM	Forest	10	.076	.061	.139	.080	.114
		20	.067	.053	.129	.071	.108
		50	.056	.044	.113	.056	.096
	LGBM	10	.073	.051	.124	.080	.113
		20	.064	.044	.114	.072	.105
		50	.053	.035	.097	.059	.093
	Ridge	10	.057	.043	.107	.075	.079
		20	.048	.035	.096	.066	.072
		50	.039	.027	.081	.053	.061
Sap flow	Forest	10	.070	.058	.107	.076	.073
		20	.062	.050	.097	.068	.067
		50	.051	.042	.082	.056	.059
	LGBM	10	.107	.060	.105	.078	.082
		20	.098	.052	.094	.069	.075
		50	.086	.045	.078	.056	.067
	Ridge	10	.097	.286	.102	.086	.404
		20	.088	.279	.089	.077	.397
		50	.075	.271	.071	.063	.390

B Theoretical Background

We denote the full dataset as $D = (D_1, \dots, D_{t+1})$, where $D_i = (X_i, Y_i)$ is the i -th datapoint. Since we are in the split conformal setting (Vovk et al., 2005), the full dataset is subdivided into two parts: the calibration and the test data. The prediction model $\hat{\mu}$ is already given in this setting and not selected based on D . The prediction interval \widehat{C}_t^α for split conformal prediction is given by

$$\widehat{C}_t^\alpha(X_{t+1}) = \hat{\mu}(X_{t+1}) \pm \mathbf{Q}_{1-\alpha} \left(\sum_{i=1}^t \frac{1}{t+1} \cdot \delta_{R_i} + \frac{1}{t+1} \cdot \delta_{+\infty} \right), \quad (11)$$

where $R_i = |Y_i - \hat{\mu}(X_i)|$, δ_c is a point mass at c , and \mathbf{Q}_τ is the τ -quantile of a distribution. Vovk et al. (2005) show that this interval provides a *marginal coverage guarantee* in case of *exchangeable* data:

Theorem B.1 (Split Conformal Prediction (Vovk et al., 2005)).

If the data points $(X_1, Y_1), \dots, (X_t, Y_t), (X_{t+1}, Y_{t+1})$ are exchangeable then the split conformal prediction set defined in (11) satisfies

$$\Pr \left\{ Y_{t+1} \in \widehat{C}_t^\alpha(X_{t+1}) \right\} \geq 1 - \alpha.$$

This seminal result cannot be directly applied to our setting, because time series are often non-exchangeable (as we discuss in the introduction) and models often exhibit locally specific errors.

The remainder of this section is split into two parts. First, we discuss the theoretical connections between the MHN retrieval and CP through the lens of Foygel Barber et al. (2022). Second, we adapt the theory of Xu & Xie (2022a) to be applicable to our regime-based setting.

For the MHN retrieval, we evoke the results of Foygel Barber et al. (2022), who introduce the concept of *non-exchangeable split conformal* prediction. Instead of treating each calibration point equally, they assign an individual weight for each point, to account for non-exchangeability. Formally, we denote the weight for the i -th point by $w_i \in [0, 1]$, $i = 1, \dots, t$; and the respective normalized weights are defined as

$$\tilde{w}_i = \frac{w_i}{w_1 + \dots + w_t + 1}, \quad i = 1, \dots, t, \quad \text{and} \quad \tilde{w}_{t+1} = \frac{1}{w_1 + \dots + w_t + 1}. \quad (12)$$

The prediction interval for non-exchangeable split conformal setting \widehat{C}_t^α is given by

$$\widehat{C}_t^\alpha(X_{t+1}) = \hat{\mu}(X_{t+1}) \pm \mathbf{Q}_{1-\alpha} \left(\sum_{i=1}^t \tilde{w}_i \cdot \delta_{R_i} + \tilde{w}_{t+1} \cdot \delta_{+\infty} \right). \quad (13)$$

Foygel Barber et al. (2022) show that non-exchangeable split conformal prediction satisfies a similar bound as exchangeable split conformal prediction, which is extended by a term that accounts for a potential *coverage gap* ΔCov . Formally we define $\Delta \text{Cov} = \alpha - \alpha^*$, where α is the specified miscoverage and α^* is the observed miscoverage.

To specify the coverage gap they use the *total variation distance* d_{TV} , which is a distance metric between two probability distributions. It is defined as

$$d_{\text{TV}}(P_1, P_2) = \sup_{A \in \mathcal{F}} |P_1(A) - P_2(A)|, \quad (14)$$

where P_1 and P_2 are arbitrary distributions defined on the space (Ω, \mathcal{F}) .

Intuitively, d_{TV} measures the largest distance between two distributions. It is connected to the widely used Kullback–Leibler divergence D_{KL} through Pinsker’s inequality (Pinsker, 1964):

$$d_{\text{TV}}(P_1, P_2) \leq \sqrt{\frac{1}{2} D_{\text{KL}}(P_1 || P_2)}. \quad (15)$$

Given this measure, Foygel Barber et al. (2022) bound the coverage of non-exchangeable split conformal prediction as follows:

Theorem B.2 (Non-exchangeable split conformal prediction (Foygel Barber et al., 2022)).
The non-exchangeable split conformal method defined in (13) satisfies

$$\Pr \left\{ Y_{t+1} \in \widehat{C}_t^\alpha(X_{t+1}) \right\} \geq (1 - \alpha) - \sum_{i=1}^t \tilde{w}_i \cdot d_{\text{TV}}(R(D), R(D^i)),$$

where $R(D) = (R_1, R_2, \dots, R_{t+1})$ denotes the sequence of absolute residuals on D and D^i denotes a sequence where the test point D_{t+1} is swapped with the i -th calibration point.

The coverage gap is represented by the rightmost term. Therefore,

$$\Delta \text{Cov} \geq - \sum_{i=1}^t \tilde{w}_i \cdot d_{\text{TV}}(R(D), R(D^i)).$$

Foygel Barber et al. (2022) prove this for the full-conformal setting, which also directly applies to the split conformal setting (as they note, too). For the sake of completeness, we state the proof of Theorem B.2 explicitly for split conformal prediction (adapted from Foygel Barber et al., 2022):

By the definition of the non-exchangeable split conformal prediction interval (13), it follows that

$$Y_{t+1} \notin \widehat{C}_t^\alpha(X_{t+1}) \iff R_{t+1} > \mathbb{Q}_{1-\alpha} \left(\sum_{i=1}^t \tilde{w}_i \cdot \delta_{R_i} + \tilde{w}_{t+1} \cdot \delta_{+\infty} \right). \quad (16)$$

Next, we show that, for a given $K \in \{1, \dots, t+1\}$,

$$\mathbb{Q}_{1-\alpha} \left(\sum_{i=1}^t \tilde{w}_i \cdot \delta_{R_i} + \tilde{w}_{t+1} \cdot \delta_{+\infty} \right) \geq \mathbb{Q}_{1-\alpha} \left(\sum_{i=1}^{t+1} \tilde{w}_i \cdot \delta_{(R(D^K))_i} \right), \quad (17)$$

by considering that

$$(R(D^K))_i = \begin{cases} R_i, & \text{if } i \neq K \text{ and } i \neq t+1, \\ R_{t+1}, & \text{if } i = K, \\ R_K, & \text{if } i = t+1. \end{cases} \quad (18)$$

In the case of $K = t+1$, this holds trivially since both sides are equivalent. In the case of $K \leq t$, we can rewrite the left-hand side of inequality (17) as

$$\begin{aligned} \sum_{i=1}^t \tilde{w}_i \cdot \delta_{R_i} + \tilde{w}_{t+1} \cdot \delta_{+\infty} &= \sum_{i=1, \dots, t; i \neq K} \tilde{w}_i \cdot \delta_{R_i} + \tilde{w}_K (\delta_{R_K} + \delta_{+\infty}) + (\tilde{w}_{t+1} - \tilde{w}_K) \delta_{+\infty}. \end{aligned}$$

The right-hand side can be similarly represented as

$$\begin{aligned} \sum_{i=1}^{t+1} \tilde{w}_i \cdot \delta_{(R(D^K))_i} &= \sum_{i=1, \dots, t; i \neq K} \tilde{w}_i \cdot \delta_{R_i} + \tilde{w}_K \delta_{R_{t+1}} + \tilde{w}_{t+1} \delta_{R_K} \\ &= \sum_{i=1, \dots, t; i \neq K} \tilde{w}_i \cdot \delta_{R_i} + \tilde{w}_K (\delta_{R_K} + \delta_{R_{t+1}}) + (\tilde{w}_{t+1} - \tilde{w}_K) \delta_{R_K}. \end{aligned}$$

By the definition of the normalized weights (12) and the assumption that $w_K \in [0, 1]$, it holds that $\tilde{w}_{t+1} \geq \tilde{w}_K$. Applying this to the rewritten forms of the left- and right-hand sides, we can see that inequality (17) holds.

Substituting the right hand side of (16) by using (17), we see that

$$Y_{t+1} \notin \widehat{C}_t^\alpha(X_{t+1}) \implies R_{t+1} > \mathbf{Q}_{1-\alpha} \left(\sum_{i=1}^{t+1} \tilde{w}_i \cdot \delta_{(R(D^K))_i} \right),$$

or equivalently by using (18):

$$Y_{t+1} \notin \widehat{C}_t^\alpha(X_{t+1}) \implies (R(D^K))_K > \mathbf{Q}_{1-\alpha} \left(\sum_{i=1}^{t+1} \tilde{w}_i \cdot \delta_{(R(D^K))_i} \right). \quad (19)$$

For the next step we use the definition of the set of so-called *strange points* \mathcal{S} :

$$\mathcal{S}(\epsilon) = \left\{ i \in [t+1] : \epsilon_i > \mathbf{Q}_{1-\alpha} \left(\sum_{j=1}^{t+1} \tilde{w}_j \cdot \delta_{\epsilon_j} \right) \right\}. \quad (20)$$

A strange point $s \in \mathcal{S}$ therefore refers to a data point with residuals that are outside the prediction interval. Given the definition of \mathcal{S} , we can directly see that

$$\sum_{i \in \mathcal{S}(\epsilon)} \tilde{w}_i \leq \alpha \text{ for all } \epsilon \in \mathbb{R}^{t+1}, \quad (21)$$

Combining (19) and (20) we see that non-coverage of Y_{t+1} implies strangeness of point K :

$$Y_{t+1} \notin \widehat{C}_t^\alpha(X_{t+1}) \implies K \in \mathcal{S}(R(D^K)). \quad (22)$$

Given this, we arrive at the final derivation of the coverage bound:

$$\begin{aligned} \Pr \{ K \in \mathcal{S}(R(D^K)) \} &= \sum_{i=1}^{t+1} \Pr \{ K = i \text{ and } i \in \mathcal{S}(R(D^i)) \} \\ &= \sum_{i=1}^{t+1} \tilde{w}_i \cdot \Pr \{ i \in \mathcal{S}(R(D^i)) \} \\ &\leq \sum_{i=1}^{t+1} \tilde{w}_i \cdot (\Pr \{ i \in \mathcal{S}(R(D)) \} + d_{\text{TV}}(R(D), R(D^i))) \\ &= \mathbb{E} \left[\sum_{i \in \mathcal{S}(R(D))} \tilde{w}_i \right] + \sum_{i=1}^t \tilde{w}_i \cdot d_{\text{TV}}(R(D), R(D^i)) \\ &\leq \alpha + \sum_{i=1}^t \tilde{w}_i \cdot d_{\text{TV}}(R(D), R(D^i)), \end{aligned}$$

where we use (21) from the penultimate to the last line. The first to the second line follows from $K \perp\!\!\!\perp D^i$, which holds because $K \perp\!\!\!\perp D$ and D^i is a permutation of D that does not depend on K .

Foygel Barber et al. (2022) show two additional variations of the coverage gap bound based on Theorem B.2. We do not replicate them here. One notable observation of theirs, however, is that instead of using the total variation distance based on the residual vectors also the distance of the raw data vector can be used:

$$\Delta \text{Cov} \geq - \sum_i \tilde{w}_i \cdot d_{\text{TV}}(D, D^i). \quad (23)$$

This coverage bound suggests that low weights for time steps corresponding to high total variation distance ensure small coverage gaps. However, lower weights weaken the estimation quality of the prediction intervals. Hence, all relevant time steps should receive high weights, while all others should receive weights close to zero.

HopCPT leverages these results by using the association weights a_i from Equation 6 to reflect the weights \tilde{w}_i of non-exchangeable split conformal prediction. HopCPT aims to assign high association weights to data points that are from the same error distribution as the current point, and low weights to data points in the opposite case. By Theorem B.2, association weights that follow this pattern lead to a small coverage gap.

An asymptotic (conditional) coverage bound If we assume clearly distinguished error distributions instead of gradually shifting ones, hard weight assignment, i.e., association weights that are either zero or one, are a meaningful choice. Given this simplification we can directly link HopCPT to the work of Xu & Xie (2022a).

Xu & Xie (2022a) introduce a variant of (split) conformal prediction with asymmetric prediction intervals:

$$\widehat{C}_t^\alpha(x_{t+1}) := \left[\hat{\mu}_{-(t+1)}(x_{t+1}) + \mathbf{Q}_{\frac{\alpha}{2}}(\{\hat{\epsilon}_i\}_{i=1}^t), \hat{\mu}_{-(t+1)}(x_{t+1}) + \mathbf{Q}_{1-\frac{\alpha}{2}}(\{\hat{\epsilon}_i\}_{i=1}^t) \right] \quad (24)$$

The approach taken by Xu & Xie (2022a) additionally adjusts the share of α between the upper and lower quantiles such that the width of the prediction interval is minimized. In contrast, HopCPT adopts a simpler strategy and uses $\frac{\alpha}{2}$ on both sides, which mitigates the need for excessive recalculation of the quantile function.

Based on the introduced interval calculation procedure, they also provide bounds regarding its coverage properties, in particular about the possible coverage gap. While Xu & Xie (2022a) base their assumption on error properties only in temporal proximity, we generalize this to proximity in the learned feature representation (which can include but is not limited to information about temporal proximity). Based on this proximity we assume:

Assumption B.3 (Error regimes). Given $\{(\mathbf{Z}_i, y_i, \hat{y}_i)\}_{i=1}^{t+1}$ which represents the (encoded) dataset and the predictions \hat{y}_i of $\hat{\mu}$, there exists a partition $\mathcal{T} = \{T_i\}_{i \in I}$ of the time steps $\{1, \dots, t\}$, so that

- (i) $\forall i \in I : \{\epsilon_t = y_t - \hat{y}_t \mid t \in T_i\} \sim E_i$,
- (ii) $\exists i \in I : \{\epsilon_{t+1}\} \sim E_i$,
- (iii) the subset T_i corresponding to $t + 1$ can be identified based on \mathbf{Z}_{t+1} ,
- (iv) $\forall i, j \in I : i = j \vee E_i \neq E_j$,

where each E_i is an arbitrary error distribution.

Properties (i) and (ii) imply that any given time step $t + 1$ can be associated to a subset T_i where all errors follow a common error distribution E_i ; property (iii) ensures that the partition can be found or approximated from a set of features. Property (iv) is not necessary for the discussion at hand but avoids degenerate solutions, since tight coverage bounds call for assigning all errors from the same error distribution to one large partition. If the errors of the associated subset were sampled i.i.d. from E_i , we could use standard split conformal methods (Vovk et al., 2005), and the variation distance between permutations of the errors in properties (i) and (ii) is zero. In practice, error noise can make it challenging to find and delineate a given partition. Thus, HopCPT uses a soft-selection approach to approximate the discrete association of a partition and the current features.

To align HopCPT with the results of Xu & Xie (2022a), and thus make use of their proposed coverage bounds for asymmetric prediction intervals, we first introduce their decomposition of the error: $\epsilon_t = \check{\epsilon}_t + (\mu(\mathbf{x}_t) - \hat{\mu}(\mathbf{x}_t))$, where f is the true generating function, $\hat{\mu}$ the prediction model, and $\check{\epsilon}$ a noise term associated with the label. The notation $\mu_{-t}(\mathbf{x})$ stems from Xu & Xie (2022a) and denotes an evaluation of μ , selected without using t .

Next, we adopt their i.i.d. assumption about the noise with regard to our approach:

Assumption B.4 (Noise is approximately *i.i.d.* within an error regime; adaptation of Xu & Xie (2022a), Assumption 1). Assume $\exists i \in I : \{\check{\epsilon}_t | t \in T_i\} \cup \{\check{\epsilon}_{t+1}\} \stackrel{\text{iid}}{\sim} E_i$ and that the CDF \check{F}_i of E_i is Lipschitz continuous with constant $L_i > 0$.

This *i.i.d.* assumption within each error regime only concerns the noise of the true generating function. Xu & Xie (2022a) note that the generating process itself can exhibit arbitrary dependence and be highly non-stationary while still having *i.i.d.* noise. The assumption is thus relatively weak.

Assumption B.5 (Estimation quality; adaptation of Xu & Xie (2022a), Assumption 2). There exist real sequences $\{\delta_{i,|T_i|}\}_{i,|T_i| \geq 1}$ such that

- (i) $\forall i \in I : \frac{1}{|T_i|} \sum_{t \in T_i} (\hat{\mu}_{-t}(\mathbf{x}_t) - \mu(\mathbf{x}_t))^2 \leq \delta_{i,|T_i|}^2$
- (ii) $\exists i \in I : |\hat{\mu}_{-(t+1)}(\mathbf{x}_{t+1}) - \mu(\mathbf{x}_{t+1})| \leq \delta_{i,|T_i|}$, where the i for a given $t + 1$ is the same i as in assumption B.4.

We want to bound the coverage of (24), which is based on the prediction error ϵ . However, Assumption B.4 only considers the noise $\check{\epsilon}$ of the true generating function. Xu & Xie (2022a) bind the difference between the CDF of the true generation function \check{F}_i , the *empirical* analogue $\tilde{F}_i(x) := \frac{1}{|T_i|} \sum_{j \in T_i} \mathbf{1}\{\check{\epsilon}_j \leq x\}$, and the empirical CDF of the prediction error $F_i(x) := \frac{1}{|T_i|} \sum_{j \in T_i} \mathbf{1}\{\epsilon_j \leq x\}$.

In particular, they state two lemmas:

Lemma B.6 (Adaptation of Xu & Xie (2022a), Lemma 1). *Under Assumption B.4, for any subset size $|T_i|$, there is an event A_T which occurs with probability at least $1 - \sqrt{\log(16|T_i|)/|T_i|}$, such that conditioning on A_T ,*

$$\sup_x |\tilde{F}_i(x) - \check{F}_i(x)| \leq \sqrt{\log(16|T_i|)/|T_i|}.$$

Lemma B.7 (Adaptation of Xu & Xie (2022a), Lemma 2). *Under Assumptions B.4 and B.5, we have*

$$\sup_x |F_i(x) - \tilde{F}_i(x)| \leq (L_i + 1)\delta_{i,|T_i|}^{2/3} + 2 \sup_x |\tilde{F}_i(x) - \check{F}_i(x)|.$$

With this result we arrive at a bound for a conditional and a marginal coverage:

Theorem B.8 (Conditional coverage gap; adaptation of Xu & Xie (2022a), Theorem 1). *Given the prediction interval \hat{C}_t^α defined in (24). Under Assumption B.4 and B.5, for any subset size $|T_i|$, $\alpha \in (0, 1)$, and $\beta \in [0, \alpha]$, we have:*

$$\begin{aligned} \exists i \in I : & \left| \Pr \left\{ Y_{t+1} \in \hat{C}_t^\alpha(X_{t+1}) | X_{t+1} = \mathbf{x}_{t+1} \right\} - (1 - \alpha) \right| \\ & \leq 12 \sqrt{\log(16|T_i|)/|T_i|} + 4(L_i + 1)(\delta_{i,|T_i|}^{2/3} + \delta_{i,|T_i|}). \end{aligned} \quad (25)$$

Furthermore, if $\{\delta_{i,|T_i|}\}_{|T_i| \geq 1}$ converges to zero, the upper bound in (25) converges to 0 when $|T_i| \rightarrow \infty$, and thus the conditional coverage is asymptotically valid.

Theorem B.9 (Marginal coverage gap; adaptation of Xu & Xie (2022a), Theorem 2). *Given the prediction interval \hat{C}_t^α defined in (24). Under Assumption B.4 and B.5, for any subset size $|T_i|$, $\alpha \in (0, 1)$, and $\beta \in [0, \alpha]$, we have:*

$$\exists i \in I : \left| \Pr \left\{ Y_{t+1} \in \hat{C}_t^\alpha(X_{t+1}) \right\} - (1 - \alpha) \right| \leq 12 \sqrt{\log(16|T_i|)/|T_i|} + 4(L_i + 1)(\delta_{i,|T_i|}^{2/3} + \delta_{i,|T_i|}).$$

The proofs of the above theorems follow from Xu & Xie (2022a). To apply our adaptations to their proofs, one has to select the error regime matching to the test time step $t + 1$, i.e., select the right subset T_i from the partitioning of time steps. T_i then corresponds to the overall calibration data in the original assumptions, lemmas, theorems, and the respective proofs. This is valid since Assumption B.5-(i) encompasses all subsets and the existing subset in Assumption B.4 and Assumption B.5-(ii) is, as noted, the same.

Xu & Xie (2022a) provide additional bounds for two variations of Assumption B.4, imposing only the requirement of strongly mixing noise or noise following a linear process. These bounds apply also to our adaptation but are omitted here for brevity.

Notes on Exchangeability, Stationarity, Seasonality, and Drifts Comparing HopCPT to standard CP we see that HopCPT assumes exchangeability over the weighted time steps within regimes. Hence, we require that the relationship between inputs and outputs remains stationary within regimes, which is weaker than requiring that the time series as such is stationary. For example, it allows that time series values decrease or grow over time as long as these changes are reflected in the inputs of the MHN and correspond to a regime. HopCPT softens the exchangeability requirements of standard CP in two ways:

1. The CP mechanism assumes that exchangeability is given within a regime that is selected by the MHN association.
2. Even if (1) is not the case, the memory of the MHN (and therefore the calibration data) is updated with each new observation. This memory update allows HopCPT to account for shifts — empirically, the benefit is visible in our experiments on the sap flow dataset, as we discuss briefly in Section 3.2 (lines 283-289) and in more detail in Appendix A.3 (Error Trend & Figure 4).

Regarding seasonality: HopCPT uses covariate features to describe the current time step. Hence, HopCPT implicitly considers seasonality by comparing a given time step with the time steps from the memory. Whenever a time step of a certain season is encountered, it focuses on time steps from the same season. In fact, our experiments already comprise both regular and irregular seasonality patterns. For example, the streamflow dataset contains yearly reoccurring patterns (spring, summer, fall, winter) as well as irregularly reoccurring similar flood events. In both cases, HopCPT can identify related time steps based on the covariates.

Regarding data drifts: an advantage of HopCPT is that the memory is updated with every new observation. Therefore, HopCPT can somewhat incorporate drifts in the target value as long as the covariates remain so that the learned representation is able to focus on the relevant observations. Empirically, the robustness against drifts is visible in our experiments on the sap flow dataset, as we discuss briefly in Section 3.2 (lines 283-289) and in more detail in Appendix A.3 (Error Trend & Figure 4).

C Dataset Details

Datasets from four different domains were used in the experiments. The following paragraphs summarize the details. Table 9 provides a quantitative overview.

Solar. We conducted experiments on three solar radiation datasets: Solar (3M), Solar (1Y), and Solar (3Y). All three datasets are based on data from the US National Solar Radiation Database (NSDB; Sengupta et al., 2018). Besides solar radiation as the target variable, the datasets include 8 other environmental features. Solar (3M) is the same dataset as used by Xu & Xie (2022a,b) and focuses on data from 8 cities in California. To show the scalability of HopCPT we additionally generated two larger datasets Solar (1Y) and Solar (3Y), which include data from 50 cities from different parts of the US. We selected the cities by ordering the areas provided by NSDB according to the population density and picked the top 50 under the condition that no city appears twice in the dataset.

Air quality. The datasets Air Quality (10PM) and Air Quality (25PM) are air quality measurements from 12 monitoring sites in Beijing, China (Zhang et al., 2017). The datasets provide two target variables (10PM and 2.5PM measurements) which we use separately in our experiments (the variables are used mutually exclusively in the datasets, e.g., when predicting 10PM we do not use 2.5PM as a feature). We encode the wind direction, given as a categorical variable, by mapping the north–south and the east–west components each to a scalar from -1 to 1 .

Sap flow. The Sap flow dataset is a subset of the Sapflux data project (Poyatos et al., 2021). This dataset includes sap flow measurements which we use as a target variable, as well as a set of environmental variables. The available features, the length of the measurements, and the sampling vary between the individual time series. To get a set of comparable time series we processed the data as follows: (a) We removed all time series where not all of the 10 environmental features are available. (b) If there was a single missing value between two existing ones, we filled the value with the value before (forward fill). (c) We cut out all sequences without any missing target or feature values (after step b). (d) From the resulting set of sequences we removed all that have less than 15,000 or more than 20,000 time steps.

Streamflow. For our experiments on the streamflow data, we use the Catchment Attributes and Meteorology for Large-sample Studies dataset (CAMELS; Newman et al., 2015; Addor et al., 2017). It provides meteorological time series from different data products, corresponding streamflow measurements, and static catchment attributes for catchments across the continental United States. We ran our experiments on the subset of 531 catchments that were used in previous hydrological benchmarking efforts (e.g., Newman et al., 2017; Kratzert et al., 2019, 2021; Klotz et al., 2022). Specifically, we trained the LSTM prediction model with the NeuralHydrology Python library (Kratzert et al., 2022) on precipitation, solar radiation, minimum and maximum temperature, and vapor pressure from the NLDAS (Xia et al., 2012), Maurer (Maurer et al., 2002), and Daymet (Thornton et al., 1997) meteorological data products. Further, the LSTM received 26 static catchment attributes at each time step that identify the catchment properties. Table 4 in Kratzert et al. (2019) provides a full list of these attributes. We trained the prediction model on data from the period Oct 1981 – Sep 1990 (note that for some catchments, this period starts later due to missing data in the beginning), calibrated the uncertainty models on Oct 1990 – Sep 1999, and tested them on the period Oct 1999 – Sep 2008.

D kNN vs. Learned Representation

As mentioned in the main paper, we designed HopCPT with large datasets in mind. It is only in such a setting that the learned part of our approach can truly play to its strengths and take advantage of nuanced interrelationships in the data. kNN provides us with a natural “fallback” option for settings where not enough data is available to infer these relationships. Our comparisons in Table 10 and Table 11 substantiate this argument: kNN provides competitive results for the small dataset Solar (3M) (this can also be seen by contrasting the performance from Table 10 to the respective results in Appendix A.3), but is outperformed by HopCPT for the larger datasets.

Table 9: Details of the evaluated datasets.

	Number of Series	Time Steps per Series	Period	Sampling	Number of Features	Data Split [%]
Solar (3M)	8	2,000	01–03 2018	60m	8	60/15/25
Solar (1Y)	50	8,760	2019	60m	8	60/15/25
Solar (3Y)	50	26,304	2018–20	60m	8	34/33/33
Air Quality (10PM)	12	35,064	2013–17	60m	11	34/33/33
Air Quality (25PM)	12	35,064	2013–17	60m	11	34/33/33
Sap flow	24	15,000–20,000	2008–16	varying	10	34/33/33
Streamflow	531	9,862	1981–2008	24h	41	34/33/33

E Quantile of Sample vs. Quantile of Weighted ECDF

HopCPT constructs prediction intervals by calculating a quantile on the set of weight-sampled errors (see Equation 7). An alternative approach is to calculate the quantile over a weighted empirical CDF of the errors. This approach would define $q(\tau, \mathbf{Z}_{t+1})$ in Equation 7 as

$$q(\tau, \mathbf{Z}_{t+1}) = \mathcal{Q}_\tau \left(\sum_{i=1}^t a_{t+1,i} \delta_{\epsilon_i} \right), \quad (26)$$

where δ_{ϵ_i} is a point mass at $|\epsilon_i|$. Empirically, we find little differences in the performance when comparing the two approaches (Tables 12 and 14).

F Asymmetrical Error Quantiles

HopCPT calculates the prediction interval by using equally large quantiles (in terms of distribution mass, not width) for the upper and lower bound (see Equation 7). Xu & Xie (2022a) instead search for a $\hat{\beta} \in [0, \alpha]$ and calculate the lower quantile with $\hat{\beta}$ and the upper quantile with $1 - \alpha + \hat{\beta}$, which minimizes the overall interval width. Applying this principle to Equation 7 one would arrive at

$$\begin{aligned} \hat{\beta} &= \operatorname{argmin}_{\beta \in [0, \alpha]} \left[\hat{\mu}(\mathbf{X}_{t+1}) + q(\beta, \mathbf{Z}_{t+1}), \hat{\mu}(\mathbf{X}_{t+1}) + q(1 - \alpha + \beta, \mathbf{Z}_{t+1}) \right] \\ \hat{C}_t^\alpha(\mathbf{Z}_{t+1}) &= \left[\hat{\mu}(\mathbf{X}_{t+1}) + q(\hat{\beta}, \mathbf{Z}_{t+1}), \hat{\mu}(\mathbf{X}_{t+1}) + q(1 - \alpha + \hat{\beta}, \mathbf{Z}_{t+1}) \right], \end{aligned} \quad (27)$$

Practically, the search is done by evaluating different β values within the potential value range and selecting the one which produces the lowest interval width. Theoretically, this could lead to more efficient intervals at the cost of additional computation and potential asymmetry in regard to uncovered samples that are higher and lower than the prediction interval. Empirically, we do not find a notable improvement when applying this search to HopCPT (see Table 13).

G AdaptiveCI and HopCPT

As noted in Section 3, AdaptiveCI is orthogonal to HopCPT, SPCI, EnbPI, and NexCP. We therefore also evaluated the combined application of the models. Nevertheless, AdaptiveCI is an independent model on top of an existing model, which is reflected in the way we select the hyperparameters of the combined model: First, the hyperparameters are selected for each model without adaption through AdaptiveCI (see Appendix A.1) — hence, we use the same hyperparameters as in the main evaluation. Second, we conduct another hyperparameter search, given the model parameters from the first search, where we only search for the parameter of the adaptive component.

Tables 15 and 16 show the results of these experiments. Overall, the results are slightly better, as the Winkler score (which considers both width and coverage) slightly improves in most experiments. The ranking between the different models stays similar to the non-adaptive comparison (see Section 3.2) with HopCPT performing best on all but the smallest dataset.

H Details on Continuous Modern Hopfield Networks

Modern Hopfield Networks are associative memory networks. They learn to associate entries of a memory with a given “query” sample in order to produce a prediction. In HopCPT, the memory corresponds to representations of past time steps and the query corresponds to a representation of the current time step. The association happens by means of weights on every memory entry, which are called “association weights”. Query–memory sample pairs that have similar representations are assigned high association weights. In summary, the association weights indicate which samples are closely related — in HopCPT, this corresponds to finding the time steps which are part of the same time series regimes and therefore useful to estimate the current uncertainty. The association mechanism is in that sense closely related to the attention mechanism of Transformers (Vaswani et al., 2017). However, compared to other trainable networks, the memory-based architecture has the advantage that it does not need to encode all knowledge in network parameters but can dynamically adapt when given new memory entries.

We adapt the following arguments from Fürst et al. (2022) and Ramsauer et al. (2021) for a more formal overview. Associative memory networks have been designed to store and retrieve samples. Hopfield networks are energy-based, binary associative memories, which were popularized as artificial neural network architectures in the 1980s (Hopfield, 1982, 1984). Their storage capacity can be considerably increased by polynomial terms in the energy function (Chen et al., 1986; Psaltis & Cheol, 1986; Baldi & Venkatesh, 1987; Gardner, 1987; Abbott & Arian, 1987; Horn & Usher, 1988; Caputo & Niemann, 2002; Krotov & Hopfield, 2016). In contrast to these binary memory networks, we use continuous associative memory networks with far higher storage capacity. These networks are continuous and differentiable, retrieve with a single update, and have exponential storage capacity (and are therefore scalable, i.e., able tackle large problems; Ramsauer et al., 2021).

Formally, we denote a set of patterns $\{\mathbf{x}_1, \dots, \mathbf{x}_N\} \subset \mathbb{R}^d$ that are stacked as columns to the matrix $\mathbf{X} = (\mathbf{x}_1, \dots, \mathbf{x}_N)$ and a state pattern (query) $\boldsymbol{\xi} \in \mathbb{R}^d$ that represents the current state. The largest norm of a stored pattern is $M = \max_i \|\mathbf{x}_i\|$. Then, the energy E of continuous Modern Hopfield Networks with state $\boldsymbol{\xi}$ is defined as (Ramsauer et al., 2021)

$$E = -\beta^{-1} \log \left(\sum_{i=1}^N \exp(\beta \mathbf{x}_i^T \boldsymbol{\xi}) \right) + \frac{1}{2} \boldsymbol{\xi}^T \boldsymbol{\xi} + C, \quad (28)$$

where $C = \beta^{-1} \log N + \frac{1}{2} M^2$. For energy E and state $\boldsymbol{\xi}$, Ramsauer et al. (2021) proved that the update rule

$$\boldsymbol{\xi}^{\text{new}} = \mathbf{X} \text{softmax}(\beta \mathbf{X}^T \boldsymbol{\xi}) \quad (29)$$

converges globally to stationary points of the energy E and coincides with the attention mechanisms of Transformers (Vaswani et al., 2017; Ramsauer et al., 2021).

The *separation* Δ_i of a pattern \mathbf{x}_i is its minimal dot product difference to any of the other patterns:

$$\Delta_i = \min_{j, j \neq i} (\mathbf{x}_i^T \mathbf{x}_i - \mathbf{x}_i^T \mathbf{x}_j). \quad (30)$$

A pattern is *well-separated* from the data if Δ_i is above a given threshold (specified in Ramsauer et al., 2021). If the patterns \mathbf{x}_i are well-separated, the update rule Equation 29 converges to a fixed point close to a stored pattern. If some patterns are similar to one another and, therefore, not well-separated, the update rule converges to a fixed point close to the mean of the similar patterns.

The update rule of a Hopfield network thus identifies sample–sample relations between stored patterns. This enables similarity-based learning methods like nearest neighbor search (see Schäfl et al., 2022), which HopCPT leverages to learn a retrieval of samples from similar error regimes.

I Potential Social Impact

Reliable uncertainty estimates are crucial, especially for complex time-dependent environmental phenomena. However, overreliance on these estimates can be dangerous. For example, unseen regimes might not be properly predicted. A changing climate that evolves the environment beyond already seen conditions can cause new forms of error regimes which cannot be predicted reliably. As most machine learning approaches, our method requires accurately labeled training data. Incorrect labels may lead to unexpected biases and prediction errors.

J Code and Data

The code and data to reproduce all of our experiments are available at <https://github.com/ml-jku/HopCPT>.

Table 10: Performance of kNN compared to HopCPT for the miscoverage $\alpha = 0.10$ on the solar datasets. The error term represents the standard deviation over repeated runs.

Data	FC	UC	kNN	HopCPT
Solar 3Y	Forest	Δ Cov	0.015	$0.029^{\pm 0.012}$
		PI-Width	97.2	$39.0^{\pm 6.2}$
		Winkler	1.59	$0.73^{\pm 0.20}$
	LGBM	Δ Cov	0.012	$0.001^{\pm 0.003}$
		PI-Width	108.4	$37.7^{\pm 0.7}$
		Winkler	1.74	$0.57^{\pm 0.01}$
	Ridge	Δ Cov	-0.009	$0.040^{\pm 0.001}$
		PI-Width	136.9	$44.9^{\pm 0.5}$
		Winkler	1.99	$0.64^{\pm 0.00}$
	LSTM	Δ Cov	-0.002	$0.001^{\pm 0.006}$
		PI-Width	22.9	$17.9^{\pm 0.6}$
		Winkler	0.51	$0.30^{\pm 0.01}$
Solar 1Y	Forest	Δ Cov	0.026	$0.047^{\pm 0.004}$
		PI-Width	66.9	$28.6^{\pm 1.0}$
		Winkler	1.00	$0.40^{\pm 0.04}$
	LGBM	Δ Cov	0.003	$-0.003^{\pm 0.009}$
		PI-Width	72.2	$40.7^{\pm 2.8}$
		Winkler	1.08	$0.57^{\pm 0.08}$
	Ridge	Δ Cov	-0.007	$-0.011^{\pm 0.016}$
		PI-Width	128.8	$59.9^{\pm 5.6}$
		Winkler	1.63	$0.92^{\pm 0.12}$
	LSTM	Δ Cov	0.000	$0.028^{\pm 0.010}$
		PI-Width	16.1	$16.0^{\pm 0.6}$
		Winkler	0.33	$0.22^{\pm 0.01}$
Solar Small	Forest	Δ Cov	0.034	$0.008^{\pm 0.006}$
		PI-Width	35.0	$38.4^{\pm 3.4}$
		Winkler	0.93	$1.09^{\pm 0.08}$
	LGBM	Δ Cov	-0.022	$0.007^{\pm 0.012}$
		PI-Width	47.2	$48.2^{\pm 1.7}$
		Winkler	1.17	$1.24^{\pm 0.08}$
	Ridge	Δ Cov	0.004	$-0.016^{\pm 0.022}$
		PI-Width	49.1	$78.2^{\pm 24.5}$
		Winkler	1.08	$1.78^{\pm 0.59}$

Table 11: Performance of kNN compared to HopCPT for the miscoverage $\alpha = 0.10$ on the different non-solar datasets. The error term represents the standard deviation over repeated runs.

Data	FC	UC	kNN	HopCPT
Air 10 PM	Forest	Δ Cov	-0.071	$0.028^{\pm 0.019}$
		PI-Width	186.3	93.9 $^{\pm 11.1}$
		Winkler	3.81	1.50 $^{\pm 0.09}$
	LGBM	Δ Cov	-0.064	$0.017^{\pm 0.016}$
		PI-Width	164.6	85.6 $^{\pm 7.4}$
		Winkler	3.42	1.45 $^{\pm 0.06}$
	Ridge	Δ Cov	-0.054	$0.010^{\pm 0.007}$
		PI-Width	114.8	79.9 $^{\pm 4.7}$
		Winkler	2.39	1.35 $^{\pm 0.06}$
	LSTM	Δ Cov	-0.031	$-0.002^{\pm 0.005}$
		PI-Width	57.2	$62.7^{\pm 1.5}$
		Winkler	1.30	$1.33^{\pm 0.01}$
Air 25 PM	Forest	Δ Cov	-0.081	$-0.024^{\pm 0.017}$
		PI-Width	158.4	48.1 $^{\pm 5.6}$
		Winkler	3.77	1.12 $^{\pm 0.05}$
	LGBM	Δ Cov	-0.073	$-0.021^{\pm 0.019}$
		PI-Width	130.4	46.8 $^{\pm 6.0}$
		Winkler	3.10	1.10 $^{\pm 0.05}$
	Ridge	Δ Cov	-0.059	$-0.005^{\pm 0.026}$
		PI-Width	97.5	49.3 $^{\pm 10.6}$
		Winkler	2.30	1.04 $^{\pm 0.11}$
	LSTM	Δ Cov	-0.033	$0.007^{\pm 0.008}$
		PI-Width	34.7	$40.7^{\pm 4.3}$
		Winkler	0.94	0.88 $^{\pm 0.05}$
Sap flow	Forest	Δ Cov	-0.056	$0.009^{\pm 0.019}$
		PI-Width	3246.1	1078.7 $^{\pm 73.7}$
		Winkler	1.00	0.30 $^{\pm 0.01}$
	LGBM	Δ Cov	-0.063	$-0.016^{\pm 0.013}$
		PI-Width	2647.5	875.5 $^{\pm 49.8}$
		Winkler	0.88	0.27 $^{\pm 0.00}$
	Ridge	Δ Cov	-0.052	$-0.025^{\pm 0.023}$
		PI-Width	2808.4	1639.6 $^{\pm 93.2}$
		Winkler	0.82	0.46 $^{\pm 0.05}$
	LSTM	Δ Cov	-0.026	$0.004^{\pm 0.004}$
		PI-Width	719.5	594.3 $^{\pm 7.7}$
		Winkler	0.24	0.19 $^{\pm 0.01}$
Streamflow	LSTM	Δ Cov	-0.108	$0.001^{\pm 0.041}$
		PI-Width	1.70	1.39 $^{\pm 0.17}$
		Winkler	1.39	0.79 $^{\pm 0.03}$

Table 12: Performance of the weighted sample quantile (Sample) and the weighted empirical CDF (ECDF) quantile strategies that HopCPT uses for the miscoverage $\alpha = 0.10$ on the solar datasets. The error term represents the standard deviation over repeated runs.

Data	FC	UC	Sample	ECDF
Solar 3Y	Forest	Δ Cov	$0.029^{\pm 0.012}$	$0.021^{\pm 0.008}$
		PI-Width	$39.0^{\pm 6.2}$	33.1 $^{\pm 1.0}$
		Winkler	$0.73^{\pm 0.20}$	0.62 $^{\pm 0.03}$
	LGBM	Δ Cov	$0.001^{\pm 0.003}$	$-0.006^{\pm 0.006}$
		PI-Width	$37.7^{\pm 0.7}$	37.1 $^{\pm 0.9}$
		Winkler	0.57 $^{\pm 0.01}$	$0.58^{\pm 0.01}$
	Ridge	Δ Cov	$0.040^{\pm 0.001}$	$0.041^{\pm 0.001}$
		PI-Width	44.9 $^{\pm 0.5}$	$45.0^{\pm 0.5}$
		Winkler	0.64 $^{\pm 0.00}$	0.64 $^{\pm 0.00}$
	LSTM	Δ Cov	$0.001^{\pm 0.006}$	$0.001^{\pm 0.006}$
		PI-Width	$17.9^{\pm 0.6}$	17.8 $^{\pm 0.4}$
		Winkler	0.30 $^{\pm 0.01}$	0.30 $^{\pm 0.00}$
Solar 1Y	Forest	Δ Cov	$0.047^{\pm 0.004}$	$0.048^{\pm 0.005}$
		PI-Width	28.6 $^{\pm 1.0}$	$28.9^{\pm 1.0}$
		Winkler	0.40 $^{\pm 0.04}$	0.40 $^{\pm 0.04}$
	LGBM	Δ Cov	$-0.003^{\pm 0.009}$	$0.000^{\pm 0.007}$
		PI-Width	$40.7^{\pm 2.8}$	40.5 $^{\pm 2.9}$
		Winkler	$0.57^{\pm 0.08}$	0.56 $^{\pm 0.08}$
	Ridge	Δ Cov	$-0.011^{\pm 0.016}$	$-0.006^{\pm 0.013}$
		PI-Width	$59.9^{\pm 5.6}$	57.5 $^{\pm 2.5}$
		Winkler	$0.92^{\pm 0.12}$	0.88 $^{\pm 0.10}$
	LSTM	Δ Cov	$0.028^{\pm 0.010}$	$0.032^{\pm 0.007}$
		PI-Width	16.0 $^{\pm 0.6}$	$16.6^{\pm 1.1}$
		Winkler	0.22 $^{\pm 0.01}$	0.22 $^{\pm 0.01}$
Solar Small	Forest	Δ Cov	$0.008^{\pm 0.006}$	$0.026^{\pm 0.023}$
		PI-Width	$38.4^{\pm 3.4}$	37.1 $^{\pm 5.7}$
		Winkler	$1.09^{\pm 0.08}$	0.99 $^{\pm 0.06}$
	LGBM	Δ Cov	$0.007^{\pm 0.012}$	$0.011^{\pm 0.013}$
		PI-Width	$48.2^{\pm 1.7}$	46.3 $^{\pm 1.3}$
		Winkler	$1.24^{\pm 0.08}$	1.16 $^{\pm 0.04}$
	Ridge	Δ Cov	$-0.016^{\pm 0.022}$	$0.012^{\pm 0.011}$
		PI-Width	78.2 $^{\pm 24.5}$	$109.0^{\pm 18.6}$
		Winkler	1.78 $^{\pm 0.59}$	$2.55^{\pm 0.38}$

Table 13: Comparison of HopCPT (a) with applying the approach proposed by (Xu & Xie, 2022a,b) to search for a β that minimizes the prediction interval width (right column), and (b) without this approach which corresponds to $\beta = \alpha/2$ (left column). The experiments are done with a miscoverage rate $\alpha = 0.1$. The error term represents the standard deviation over repeated runs.

Data	FC	UC	$\beta = \alpha/2$	With β search
Solar 3Y	Forest	Δ Cov	0.029 \pm 0.012	0.010 \pm 0.018
		PI-Width	39.0 \pm 6.2	41.0 \pm 7.6
		Winkler	0.73 \pm 0.20	0.86 \pm 0.22
	LGBM	Δ Cov	0.001 \pm 0.003	-0.013 \pm 0.003
		PI-Width	37.7 \pm 0.7	36.8 \pm 6.2
		Winkler	0.57 \pm 0.01	0.62 \pm 0.12
	Ridge	Δ Cov	0.040 \pm 0.001	0.021 \pm 0.015
		PI-Width	44.9 \pm 0.5	50.0 \pm 28.3
		Winkler	0.64 \pm 0.00	0.77 \pm 0.43
	LSTM	Δ Cov	0.001 \pm 0.006	-0.013 \pm 0.007
		PI-Width	17.9 \pm 0.6	16.2 \pm 0.5
		Winkler	0.30 \pm 0.01	0.31 \pm 0.00
Air 10 PM	Forest	Δ Cov	0.028 \pm 0.019	0.007 \pm 0.028
		PI-Width	93.9 \pm 11.1	83.4 \pm 11.2
		Winkler	1.50 \pm 0.09	1.49 \pm 0.07
	LGBM	Δ Cov	0.017 \pm 0.016	-0.000 \pm 0.016
		PI-Width	85.6 \pm 7.4	77.3 \pm 6.0
		Winkler	1.45 \pm 0.06	1.41 \pm 0.04
	Ridge	Δ Cov	0.010 \pm 0.007	-0.001 \pm 0.007
		PI-Width	79.9 \pm 4.7	74.6 \pm 1.6
		Winkler	1.35 \pm 0.06	1.32 \pm 0.02
	LSTM	Δ Cov	-0.002 \pm 0.005	-0.006 \pm 0.007
		PI-Width	62.7 \pm 1.5	60.9 \pm 2.3
		Winkler	1.33 \pm 0.01	1.33 \pm 0.02
Sap flow	Forest	Δ Cov	0.009 \pm 0.019	-0.044 \pm 0.025
		PI-Width	1078.7 \pm 73.7	857.2 \pm 56.7
		Winkler	0.30 \pm 0.01	0.30 \pm 0.01
	LGBM	Δ Cov	-0.016 \pm 0.013	-0.095 \pm 0.007
		PI-Width	875.5 \pm 49.8	690.9 \pm 31.0
		Winkler	0.27 \pm 0.00	0.28 \pm 0.01
	Ridge	Δ Cov	-0.025 \pm 0.023	-0.050 \pm 0.020
		PI-Width	1639.6 \pm 93.2	1389.0 \pm 128.0
		Winkler	0.46 \pm 0.05	0.42 \pm 0.03
	LSTM	Δ Cov	0.004 \pm 0.004	-0.003 \pm 0.003
		PI-Width	594.3 \pm 7.7	557.8 \pm 8.9
		Winkler	0.19 \pm 0.01	0.19 \pm 0.00

Table 14: Performance of the weighted sample quantile (Sample) and the weighted empirical CDF (ECDF) quantile strategies that HopCPT uses for the miscoverage $\alpha = 0.10$ on the different non-solar datasets. The error term represents the standard deviation over repeated runs.

Data	FC	UC	Sample	ECDF
Air 10 PM	Forest	Δ Cov	$0.028^{\pm 0.019}$	$0.027^{\pm 0.021}$
		PI-Width	$93.9^{\pm 11.1}$	$93.4^{\pm 11.0}$
		Winkler	$1.50^{\pm 0.09}$	$1.50^{\pm 0.09}$
	LGBM	Δ Cov	$0.017^{\pm 0.016}$	$0.014^{\pm 0.015}$
		PI-Width	$85.6^{\pm 7.4}$	$84.5^{\pm 8.3}$
		Winkler	$1.45^{\pm 0.06}$	$1.43^{\pm 0.09}$
	Ridge	Δ Cov	$0.010^{\pm 0.007}$	$0.013^{\pm 0.010}$
		PI-Width	$79.9^{\pm 4.7}$	$79.3^{\pm 4.6}$
		Winkler	$1.35^{\pm 0.06}$	$1.34^{\pm 0.05}$
	LSTM	Δ Cov	$-0.002^{\pm 0.005}$	$-0.005^{\pm 0.010}$
		PI-Width	$62.7^{\pm 1.5}$	$65.6^{\pm 20.1}$
		Winkler	$1.33^{\pm 0.01}$	$1.35^{\pm 0.15}$
Air 25 PM	Forest	Δ Cov	$-0.024^{\pm 0.017}$	$-0.024^{\pm 0.019}$
		PI-Width	$48.1^{\pm 5.6}$	$47.7^{\pm 4.5}$
		Winkler	$1.12^{\pm 0.05}$	$1.11^{\pm 0.01}$
	LGBM	Δ Cov	$-0.021^{\pm 0.019}$	$-0.023^{\pm 0.019}$
		PI-Width	$46.8^{\pm 6.0}$	$46.6^{\pm 6.1}$
		Winkler	$1.10^{\pm 0.05}$	$1.10^{\pm 0.05}$
	Ridge	Δ Cov	$-0.005^{\pm 0.026}$	$-0.007^{\pm 0.027}$
		PI-Width	$49.3^{\pm 10.6}$	$49.1^{\pm 10.7}$
		Winkler	$1.04^{\pm 0.11}$	$1.04^{\pm 0.11}$
	LSTM	Δ Cov	$0.007^{\pm 0.008}$	$-0.002^{\pm 0.015}$
		PI-Width	$40.7^{\pm 4.3}$	$35.0^{\pm 2.1}$
		Winkler	$0.88^{\pm 0.05}$	$0.82^{\pm 0.05}$
Sap flow	Forest	Δ Cov	$0.009^{\pm 0.019}$	$0.011^{\pm 0.019}$
		PI-Width	$1078.7^{\pm 73.7}$	$1082.3^{\pm 74.0}$
		Winkler	$0.30^{\pm 0.01}$	$0.30^{\pm 0.01}$
	LGBM	Δ Cov	$-0.016^{\pm 0.013}$	$-0.017^{\pm 0.013}$
		PI-Width	$875.5^{\pm 49.8}$	$875.6^{\pm 49.5}$
		Winkler	$0.27^{\pm 0.00}$	$0.27^{\pm 0.00}$
	Ridge	Δ Cov	$-0.025^{\pm 0.023}$	$-0.035^{\pm 0.046}$
		PI-Width	$1639.6^{\pm 93.2}$	$1634.0^{\pm 90.2}$
		Winkler	$0.46^{\pm 0.05}$	$0.50^{\pm 0.13}$
	LSTM	Δ Cov	$0.004^{\pm 0.004}$	$0.005^{\pm 0.003}$
		PI-Width	$594.3^{\pm 7.7}$	$592.0^{\pm 9.7}$
		Winkler	$0.19^{\pm 0.01}$	$0.19^{\pm 0.00}$
Streamflow	LSTM	Δ Cov	$0.001^{\pm 0.041}$	$0.028^{\pm 0.002}$
		PI-Width	$1.39^{\pm 0.17}$	$1.49^{\pm 0.02}$
		Winkler	$0.79^{\pm 0.03}$	$0.77^{\pm 0.01}$

Table 15: Performance of the CP algorithms HopCPT, SPCI, EnbPI, and NexCP, each combined with AdaptiveCI, for the miscoverage $\alpha = 0.10$ on the solar datasets. Bold numbers correspond to the best result for the respective metric in the experiment (PI-Width and Winkler score). The error term represents the standard deviation over repeated runs. † combined with AdaptiveCI.

UC		HopCPT †	SPCI †	EnbPI †	NexCP †	CopulaCPTS †	CP/CF-RNN †	
Solar 3Y	Forest	Δ Cov	$0.004^{\pm 0.001}$	$0.002^{\pm 0.000}$	-0.001	-0.000	0.000	0.000
		PI-Width	29.8 $^{\pm 0.7}$	$97.6^{\pm 0.1}$	155.7	170.8	168.6	168.5
		Winkler	0.59 $^{\pm 0.03}$	$1.69^{\pm 0.00}$	2.43	2.54	2.52	2.52
	LGBM	Δ Cov	$-0.001^{\pm 0.000}$	$0.002^{\pm 0.000}$	-0.001	-0.000	0.000	0.000
		PI-Width	39.9 $^{\pm 7.0}$	$95.8^{\pm 0.1}$	155.0	164.8	162.3	162.4
		Winkler	0.62 $^{\pm 0.10}$	$1.70^{\pm 0.00}$	2.49	2.57	2.54	2.54
	Ridge	Δ Cov	$0.002^{\pm 0.000}$	$-0.000^{\pm 0.000}$	-0.006	0.000	0.000	-0.000
		PI-Width	36.0 $^{\pm 0.3}$	$110.6^{\pm 0.1}$	166.3	177.3	172.8	172.4
		Winkler	0.62 $^{\pm 0.00}$	$1.77^{\pm 0.00}$	2.28	2.63	2.61	2.58
	LSTM	Δ Cov	$0.000^{\pm 0.000}$	$0.001^{\pm 0.000}$	-0.002	-0.000	0.001	0.001
		PI-Width	17.8 $^{\pm 0.2}$	$25.5^{\pm 0.0}$	30.6	30.6	28.8	28.8
		Winkler	0.30 $^{\pm 0.00}$	$0.59^{\pm 0.00}$	0.63	0.62	0.63	0.63
Solar 1Y	Forest	Δ Cov	$0.007^{\pm 0.001}$	$0.011^{\pm 0.000}$	-0.002	-0.001	0.002	0.003
		PI-Width	21.5 $^{\pm 1.2}$	$72.6^{\pm 0.1}$	109.5	126.7	128.9	129.5
		Winkler	0.40 $^{\pm 0.02}$	$1.14^{\pm 0.00}$	1.63	1.85	1.84	1.84
	LGBM	Δ Cov	$0.000^{\pm 0.001}$	$0.005^{\pm 0.000}$	-0.001	-0.000	0.002	0.003
		PI-Width	41.6 $^{\pm 1.9}$	$69.2^{\pm 0.2}$	106.2	117.1	119.1	119.4
		Winkler	0.56 $^{\pm 0.04}$	$1.15^{\pm 0.00}$	1.63	1.78	1.77	1.77
	Ridge	Δ Cov	$-0.003^{\pm 0.005}$	$0.004^{\pm 0.000}$	-0.002	-0.000	-0.000	-0.000
		PI-Width	61.5 $^{\pm 9.9}$	$98.9^{\pm 0.2}$	167.8	174.8	174.9	175.6
		Winkler	0.87 $^{\pm 0.11}$	$1.32^{\pm 0.00}$	2.01	2.08	2.08	2.08
	LSTM	Δ Cov	$0.001^{\pm 0.000}$	$0.003^{\pm 0.000}$	-0.001	-0.001	0.001	0.001
		PI-Width	14.3 $^{\pm 0.7}$	$18.9^{\pm 0.0}$	21.8	20.4	19.9	20.0
		Winkler	0.22 $^{\pm 0.01}$	$0.40^{\pm 0.00}$	0.42	0.41	0.41	0.41
Solar Small	Forest	Δ Cov	$0.006^{\pm 0.003}$	$-0.023^{\pm 0.002}$	-0.003	-0.014	-0.007	-0.009
		PI-Width	33.6 $^{\pm 2.9}$	$64.7^{\pm 0.7}$	92.9	127.3	131.1	128.1
		Winkler	1.01 $^{\pm 0.04}$	$1.95^{\pm 0.01}$	2.38	3.27	3.25	3.23
	LGBM	Δ Cov	$-0.001^{\pm 0.002}$	$-0.015^{\pm 0.001}$	-0.005	-0.005	-0.008	-0.010
		PI-Width	44.8 $^{\pm 1.0}$	$60.9^{\pm 0.6}$	96.4	135.7	128.3	125.0
		Winkler	1.18 $^{\pm 0.04}$	$1.95^{\pm 0.01}$	2.54	3.32	3.33	3.31
	Ridge	Δ Cov	$0.008^{\pm 0.004}$	$-0.015^{\pm 0.001}$	-0.003	0.008	0.008	0.006
		PI-Width	$104.7^{\pm 19.8}$	69.3 $^{\pm 0.7}$	102.5	97.7	96.2	93.0
		Winkler	$2.44^{\pm 0.42}$	1.92 $^{\pm 0.01}$	2.56	2.75	2.75	2.72

Table 16: Performance of the CP algorithms HopCPT, SPCI, EnbPI, and NexCP, each combined with AdaptiveCI, for the miscoverage $\alpha = 0.10$ on the different non-solar datasets. Bold numbers correspond to the best result for the respective metric in the experiment (PI-Width and Winkler score). The error term represents the standard deviation over repeated runs. † combined with AdaptiveCI.

		UC	HopCPT †	SPCI †	EnbPI †	NexCP †	CopulaCPTS †	CP/CF-RNN †
Air 10 PM	Forest	Δ Cov	0.002 \pm 0.001	-0.002 \pm 0.000	-0.002	0.000	-0.003	-0.005
		PI-Width	80.7 \pm 2.6	112.6 \pm 0.1	250.4	270.5	228.7	228.3
		Winkler	1.45 \pm 0.06	1.96 \pm 0.00	3.70	3.92	3.37	3.39
	LGBM	Δ Cov	0.001 \pm 0.001	0.001 \pm 0.000	-0.001	0.000	-0.002	-0.003
		PI-Width	78.5 \pm 2.2	102.5 \pm 0.2	220.0	233.2	196.3	196.3
		Winkler	1.38 \pm 0.04	1.83 \pm 0.00	3.38	3.54	3.01	3.01
	Ridge	Δ Cov	0.001 \pm 0.001	0.000 \pm 0.000	-0.001	0.001	0.000	0.000
		PI-Width	75.3 \pm 0.8	83.7 \pm 0.1	147.2	159.5	142.7	142.3
		Winkler	1.30 \pm 0.02	1.46 \pm 0.00	2.46	2.67	2.41	2.42
	LSTM	Δ Cov	-0.001 \pm 0.000	0.000 \pm 0.000	0.000	0.001	0.001	0.000
		PI-Width	65.4 \pm 0.3	59.2 \pm 0.1	69.2	65.7	62.9	62.5
		Winkler	1.30 \pm 0.01	1.18 \pm 0.00	1.32	1.29	1.29	1.30
Air 25 PM	Forest	Δ Cov	-0.001 \pm 0.001	-0.002 \pm 0.000	-0.003	-0.001	-0.004	-0.008
		PI-Width	53.4 \pm 1.1	86.5 \pm 0.1	221.7	245.1	205.2	200.8
		Winkler	1.10 \pm 0.02	1.76 \pm 0.00	3.68	3.97	3.43	3.47
	LGBM	Δ Cov	-0.000 \pm 0.001	0.000 \pm 0.000	-0.001	0.000	-0.003	-0.007
		PI-Width	52.5 \pm 1.7	76.1 \pm 0.1	180.6	191.7	151.1	147.2
		Winkler	1.10 \pm 0.05	1.69 \pm 0.00	3.17	3.38	2.73	2.74
	Ridge	Δ Cov	-0.000 \pm 0.001	-0.001 \pm 0.000	-0.001	0.001	0.001	0.000
		PI-Width	50.4 \pm 3.9	63.2 \pm 0.1	130.0	143.6	130.3	129.5
		Winkler	1.04 \pm 0.10	1.33 \pm 0.00	2.36	2.64	2.53	2.52
	LSTM	Δ Cov	-0.001 \pm 0.001	-0.001 \pm 0.000	0.000	0.001	-0.001	-0.000
		PI-Width	40.3 \pm 4.1	36.3 \pm 0.0	44.6	40.8	38.8	38.9
		Winkler	0.89 \pm 0.06	0.89 \pm 0.00	0.96	0.94	0.95	0.93
Sap flow	Forest	Δ Cov	-0.004 \pm 0.007	0.004 \pm 0.000	-0.006	0.000	0.004	0.003
		PI-Width	1006.9 \pm 44.5	1651.0 \pm 1.9	4142.8	6151.7	6034.6	6022.0
		Winkler	0.29 \pm 0.01	0.51 \pm 0.00	1.11	1.54	1.53	1.53
	LGBM	Δ Cov	-0.001 \pm 0.003	0.007 \pm 0.000	-0.005	-0.000	0.006	0.008
		PI-Width	919.1 \pm 25.8	1601.7 \pm 3.0	3327.0	4845.1	4787.0	5016.1
		Winkler	0.26 \pm 0.01	0.45 \pm 0.00	0.88	1.23	1.22	1.28
	Ridge	Δ Cov	-0.006 \pm 0.002	-0.121 \pm 0.000	-0.003	-0.000	-0.004	-0.126
		PI-Width	1492.5 \pm 29.9	2974.7 \pm 6.9	3431.4	10665.6	10426.2	9521.9
		Winkler	0.39 \pm 0.01	1.53 \pm 0.00	0.87	2.39	2.36	2.87
	LSTM	Δ Cov	0.000 \pm 0.000	0.002 \pm 0.000	-0.001	-0.000	0.001	0.002
		PI-Width	595.0 \pm 7.5	639.5 \pm 1.8	863.1	1019.1	980.1	992.6
		Winkler	0.19 \pm 0.00	0.22 \pm 0.00	0.28	0.32	0.31	0.32

Table 17: Performance of the evaluated CP algorithms on the Solar (3Y) datasets for the miscoverage levels $\alpha \in \{0.05, 0.10, 0.15\}$. The column FC specifies the prediction algorithm used for the experiment (Forest: Random Forest, LGBM: LightGBM, Ridge: Ridge Regression, LSTM: LSTM neural network). Bold numbers correspond to the best result for the respective metric in the experiment (PI-Width and Winkler score), given that $\Delta\text{Cov} \geq -0.25\alpha$, i.e., the specific algorithm reached at least approximate coverage (the result is grayed out otherwise). The error term represents the standard deviation over repeated runs (results without an error term are from deterministic models).

FC	α		HopCPT	SPCI	EnbPI	NexCP	CopulaCPTS	CP/CF-RNN	AdaptiveCI
Forest	0.05	Δ Cov	0.006 \pm 0.006	0.007 \pm 0.000	-0.030	-0.002	0.002	0.002	
		PI-Width	47.8 \pm 9.5	149.2 \pm 0.1	173.0	216.5	237.2	236.7	
		Winkler	0.99 \pm 0.35	2.22 \pm 0.00	3.01	2.95	3.30	3.30	
	0.10	Δ Cov	0.029 \pm 0.012	0.012 \pm 0.000	-0.031	-0.002	0.005	0.004	
		PI-Width	39.0 \pm 6.2	103.1 \pm 0.1	131.1	166.6	174.9	174.6	
		Winkler	0.73 \pm 0.20	1.74 \pm 0.00	2.47	2.53	2.75	2.76	
	0.15	Δ Cov	0.052 \pm 0.018	0.014 \pm 0.000	-0.027	-0.002	0.006	0.006	
		PI-Width	33.6 \pm 4.6	75.3 \pm 0.1	101.4	129.1	132.2	132.0	
		Winkler	0.61 \pm 0.15	1.46 \pm 0.00	2.12	2.23	2.38	2.39	
LGBM	0.05	Δ Cov	-0.008 \pm 0.002	0.007 \pm 0.000	-0.022	-0.002	0.002	0.002	0.001
		PI-Width	45.6 \pm 0.8	148.0 \pm 0.1	183.0	215.9	237.9	237.8	88.1
		Winkler	0.72 \pm 0.02	2.25 \pm 0.00	3.09	3.06	3.45	3.46	1.36
	0.10	Δ Cov	0.001 \pm 0.003	0.014 \pm 0.000	-0.023	-0.002	0.006	0.006	0.001
		PI-Width	37.7 \pm 0.7	102.2 \pm 0.1	133.6	159.9	169.8	170.2	67.1
		Winkler	0.57 \pm 0.01	1.75 \pm 0.00	2.52	2.55	2.80	2.81	1.19
	0.15	Δ Cov	0.009 \pm 0.003	0.017 \pm 0.000	-0.022	-0.002	0.008	0.009	0.001
		PI-Width	32.7 \pm 0.7	75.5 \pm 0.1	100.6	121.3	126.6	127.2	55.1
		Winkler	0.50 \pm 0.01	1.46 \pm 0.00	2.15	2.21	2.39	2.40	1.11
Ridge	0.05	Δ Cov	0.010 \pm 0.001	-0.003 \pm 0.000	-0.080	-0.002	0.003	0.003	
		PI-Width	52.7 \pm 0.6	146.3 \pm 0.0	151.0	226.2	223.8	224.8	
		Winkler	0.78 \pm 0.00	2.31 \pm 0.00	3.04	3.20	3.44	3.46	
	0.10	Δ Cov	0.040 \pm 0.001	0.002 \pm 0.000	-0.074	-0.001	0.004	0.005	
		PI-Width	44.9 \pm 0.5	108.2 \pm 0.0	131.1	171.0	166.0	167.7	
		Winkler	0.64 \pm 0.00	1.82 \pm 0.00	2.49	2.66	2.73	2.74	
	0.15	Δ Cov	0.070 \pm 0.001	0.009 \pm 0.000	-0.069	-0.000	0.004	0.006	
		PI-Width	39.6 \pm 0.5	89.4 \pm 0.0	114.7	142.2	141.2	142.7	
		Winkler	0.56 \pm 0.00	1.56 \pm 0.00	2.21	2.34	2.37	2.37	
LSTM	0.05	Δ Cov	-0.003 \pm 0.005	0.004 \pm 0.000	-0.018	-0.001	0.002	0.001	
		PI-Width	22.7 \pm 0.8	47.7 \pm 0.0	41.0	47.3	54.1	54.7	
		Winkler	0.38 \pm 0.01	0.87 \pm 0.00	0.90	0.87	0.96	0.97	
	0.10	Δ Cov	0.001 \pm 0.006	0.014 \pm 0.000	-0.018	-0.001	0.007	0.007	
		PI-Width	17.9 \pm 0.6	27.8 \pm 0.0	24.6	28.2	31.9	33.0	
		Winkler	0.30 \pm 0.01	0.62 \pm 0.00	0.64	0.63	0.68	0.70	
	0.15	Δ Cov	0.002 \pm 0.007	0.024 \pm 0.000	-0.017	-0.001	0.010	0.009	
		PI-Width	15.0 \pm 0.4	18.1 \pm 0.0	16.2	18.6	20.5	21.3	
		Winkler	0.26 \pm 0.00	0.48 \pm 0.00	0.50	0.50	0.54	0.55	

Table 18: Performance of the evaluated CP algorithms on the Solar (1Y) dataset for the miscoverage levels $\alpha \in \{0.05, 0.10, 0.15\}$. The column FC specifies the prediction algorithm used for the experiment (Forest: Random Forest, LGBM: LightGBM, Ridge: Ridge Regression, LSTM: LSTM neural network). Bold numbers correspond to the best result for the respective metric in the experiment (PI-Width and Winkler score), given that $\Delta\text{Cov} \geq -0.25\alpha$, i.e., the specific algorithm reached at least approximate coverage (the result is grayed out otherwise). The error term represents the standard deviation over repeated runs (results without an error term are from deterministic models).

FC	α		HopCPT	SPCI	EnbPI	NexCP	CopulaCPTS	CP/CF-RNN	AdaptiveCI
Forest	0.05	Δ Cov	0.016 \pm 0.002	0.029 \pm 0.000	-0.017	0.002	0.034	0.035	
		PI-Width	35.0 \pm 1.2	147.8 \pm 0.3	133.4	173.9	241.8	262.9	
		Winkler	0.50 \pm 0.05	1.71 \pm 0.00	1.97	2.18	2.61	2.82	
	0.10	Δ Cov	0.047 \pm 0.004	0.045 \pm 0.000	-0.018	0.002	0.056	0.063	
		PI-Width	28.6 \pm 1.0	97.1 \pm 0.2	98.8	127.8	182.4	204.9	
		Winkler	0.40 \pm 0.04	1.26 \pm 0.00	1.65	1.84	2.10	2.30	
	0.15	Δ Cov	0.078 \pm 0.006	0.052 \pm 0.000	-0.016	0.002	0.070	0.086	
		PI-Width	24.6 \pm 0.8	67.7 \pm 0.1	73.1	93.6	138.5	161.2	
		Winkler	0.35 \pm 0.03	1.00 \pm 0.00	1.42	1.59	1.76	1.93	
LGBM	0.05	Δ Cov	-0.010 \pm 0.006	0.029 \pm 0.000	-0.019	0.001	0.034	0.036	-0.000
		PI-Width	51.0 \pm 3.4	147.8 \pm 0.2	131.5	165.0	237.9	265.2	62.2
		Winkler	0.71 \pm 0.10	1.72 \pm 0.00	2.05	2.16	2.60	2.86	0.78
	0.10	Δ Cov	-0.003 \pm 0.009	0.045 \pm 0.000	-0.017	0.002	0.056	0.065	0.000
		PI-Width	40.7 \pm 2.8	96.5 \pm 0.2	93.9	118.0	171.1	196.6	49.5
		Winkler	0.57 \pm 0.08	1.26 \pm 0.00	1.65	1.78	2.02	2.24	0.69
	0.15	Δ Cov	0.001 \pm 0.012	0.053 \pm 0.000	-0.014	0.002	0.068	0.086	0.000
		PI-Width	34.5 \pm 2.5	68.0 \pm 0.1	68.2	85.7	125.5	149.1	42.5
		Winkler	0.50 \pm 0.07	1.01 \pm 0.00	1.40	1.52	1.66	1.83	0.67
Ridge	0.05	Δ Cov	-0.025 \pm 0.012	0.018 \pm 0.000	-0.025	-0.004	0.008	0.011	
		PI-Width	70.3 \pm 6.5	151.0 \pm 0.2	178.0	196.3	207.9	219.8	
		Winkler	1.15 \pm 0.18	1.78 \pm 0.00	2.26	2.29	2.35	2.49	
	0.10	Δ Cov	-0.011 \pm 0.016	0.031 \pm 0.000	-0.031	-0.006	-0.010	-0.015	
		PI-Width	59.9 \pm 5.6	112.8 \pm 0.1	158.4	171.7	171.7	172.0	
		Winkler	0.92 \pm 0.12	1.40 \pm 0.00	2.06	2.09	2.12	2.17	
	0.15	Δ Cov	0.000 \pm 0.020	0.035 \pm 0.001	-0.034	-0.008	-0.024	-0.040	
		PI-Width	52.9 \pm 4.9	92.5 \pm 0.1	144.1	154.6	150.2	146.6	
		Winkler	0.81 \pm 0.10	1.21 \pm 0.00	1.92	1.96	1.98	2.02	
LSTM	0.05	Δ Cov	0.019 \pm 0.003	0.006 \pm 0.000	-0.018	-0.001	0.010	0.013	
		PI-Width	21.4 \pm 0.7	37.0 \pm 0.0	29.5	33.6	39.4	42.2	
		Winkler	0.27 \pm 0.01	0.58 \pm 0.00	0.60	0.57	0.59	0.61	
	0.10	Δ Cov	0.028 \pm 0.010	0.018 \pm 0.000	-0.018	-0.001	0.018	0.025	
		PI-Width	16.0 \pm 0.6	22.5 \pm 0.0	17.4	19.5	23.1	25.0	
		Winkler	0.22 \pm 0.01	0.41 \pm 0.00	0.42	0.41	0.43	0.43	
	0.15	Δ Cov	0.029 \pm 0.017	0.032 \pm 0.000	-0.014	0.001	0.030	0.040	
		PI-Width	13.1 \pm 0.5	15.3 \pm 0.0	11.1	12.6	15.2	16.9	
		Winkler	0.19 \pm 0.00	0.32 \pm 0.00	0.33	0.33	0.33	0.34	

Table 19: Performance of the evaluated CP algorithms on the Solar (3M) dataset for the miscoverage levels $\alpha \in \{0.05, 0.10, 0.15\}$. The column FC specifies the prediction algorithm used for the experiment (Forest: Random Forest, LGBM: LightGBM, Ridge: Ridge Regression). Bold numbers correspond to the best result for the respective metric in the experiment (PI-Width and Winkler score), given that $\Delta\text{Cov} \geq -0.25\alpha$, i.e., the specific algorithm reached at least approximate coverage (the result is grayed out otherwise). The error term represents the standard deviation over repeated runs (results without an error term are from deterministic models).

FC	α		HopCPT	SPCI	EmbPI	NexCP	CopulaCPTS	CP/CF-RNN	AdaptiveCI
Forest	0.05	Δ Cov	-0.002 \pm 0.005	-0.074 \pm 0.001	-0.022	-0.013	-0.022	-0.028	
		PI-Width	47.5 \pm 5.0	57.9 \pm 0.3	110.7	160.2	162.0	155.0	
		Winkler	1.29 \pm 0.11	2.62 \pm 0.02	2.92	3.70	3.95	4.04	
	0.10	Δ Cov	0.008 \pm 0.006	-0.064 \pm 0.002	-0.022	-0.021	-0.027	-0.025	
		PI-Width	38.4 \pm 3.4	38.8 \pm 0.3	86.0	122.9	110.4	111.4	
		Winkler	1.09 \pm 0.08	1.82 \pm 0.01	2.54	3.28	3.47	3.48	
	0.15	Δ Cov	0.020 \pm 0.010	-0.052 \pm 0.002	-0.028	-0.019	-0.020	-0.017	
		PI-Width	32.6 \pm 2.8	26.7 \pm 0.3	64.8	91.0	77.5	79.6	
		Winkler	0.99 \pm 0.07	1.45 \pm 0.02	2.40	2.91	2.99	2.98	
LGBM	0.05	Δ Cov	0.002 \pm 0.008	-0.063 \pm 0.001	-0.024	-0.014	-0.018	-0.019	-0.000
		PI-Width	59.7 \pm 3.4	56.3 \pm 0.3	111.7	161.7	164.5	162.1	61.8
		Winkler	1.49 \pm 0.15	2.66 \pm 0.02	3.10	3.87	4.13	4.18	1.45
	0.10	Δ Cov	0.007 \pm 0.012	-0.052 \pm 0.002	-0.022	-0.020	-0.022	-0.021	-0.004
		PI-Width	48.2 \pm 1.7	37.5 \pm 0.3	84.3	119.9	107.6	106.9	49.2
		Winkler	1.24 \pm 0.08	1.84 \pm 0.01	2.67	3.35	3.52	3.53	1.26
	0.15	Δ Cov	0.005 \pm 0.016	-0.043 \pm 0.002	-0.024	-0.019	-0.013	-0.011	-0.007
		PI-Width	41.4 \pm 1.3	26.9 \pm 0.2	60.8	85.1	75.8	77.5	44.1
		Winkler	1.11 \pm 0.07	1.47 \pm 0.01	2.48	2.93	2.98	2.97	1.22
Ridge	0.05	Δ Cov	-0.017 \pm 0.014	-0.064 \pm 0.001	-0.021	0.004	0.009	-0.002	
		PI-Width	92.7 \pm 32.4	67.2 \pm 0.3	110.1	144.8	156.1	133.6	
		Winkler	1.99 \pm 0.69	2.49 \pm 0.02	3.07	3.82	3.78	3.75	
	0.10	Δ Cov	-0.016 \pm 0.022	-0.056 \pm 0.002	-0.020	0.007	0.014	-0.003	
		PI-Width	78.2 \pm 24.5	51.8 \pm 0.3	84.9	85.2	88.6	78.1	
		Winkler	1.78 \pm 0.59	1.91 \pm 0.01	2.66	2.85	2.83	2.81	
	0.15	Δ Cov	-0.009 \pm 0.021	-0.039 \pm 0.002	-0.017	0.003	0.014	0.003	
		PI-Width	67.4 \pm 19.0	43.2 \pm 0.2	71.6	70.9	71.9	70.7	
		Winkler	1.61 \pm 0.51	1.59 \pm 0.00	2.29	2.34	2.34	2.33	

Table 20: Performance of the evaluated CP algorithms on the Air Quality (10PM) dataset for the miscoverage levels $\alpha \in \{0.05, 0.10, 0.15\}$. The column FC specifies the prediction algorithm used for the experiment (Forest: Random Forest, LGBM: LightGBM, Ridge: Ridge Regression, LSTM: LSTM neural network). Bold numbers correspond to the best result for the respective metric in the experiment (PI-Width and Winkler score), given that $\Delta\text{Cov} \geq -0.25\alpha$, i.e., the specific algorithm reached at least approximate coverage (the result is grayed out otherwise). The error term represents the standard deviation over repeated runs (results without an error term are from deterministic models).

FC	α		HopCPT	SPCI	EnbPI	NexCP	CopulaCPTS	CP/CF-RNN	AdaptiveCI
Forest	0.05	Δ Cov	0.006 \pm 0.013	-0.001 \pm 0.000	-0.054	-0.005	-0.016	-0.027	
		PI-Width	116.7 \pm 14.4	152.7 \pm 0.1	242.9	321.5	322.5	297.1	
		Winkler	1.94 \pm 0.10	2.86 \pm 0.00	4.97	4.82	6.47	6.61	
	0.10	Δ Cov	0.028 \pm 0.019	0.008 \pm 0.000	-0.066	-0.004	-0.019	-0.033	
		PI-Width	93.9 \pm 11.1	118.5 \pm 0.1	202.8	263.5	243.1	229.8	
		Winkler	1.50 \pm 0.09	2.23 \pm 0.00	4.16	4.03	4.94	4.98	
	0.15	Δ Cov	0.050 \pm 0.025	0.018 \pm 0.000	-0.073	-0.002	-0.021	-0.039	
		PI-Width	80.5 \pm 9.4	99.8 \pm 0.1	175.7	229.4	207.1	198.2	
		Winkler	1.28 \pm 0.08	1.92 \pm 0.00	3.72	3.61	4.18	4.20	
LGBM	0.05	Δ Cov	-0.000 \pm 0.011	0.008 \pm 0.000	-0.047	-0.005	-0.014	-0.022	-0.000
		PI-Width	106.3 \pm 9.9	146.1 \pm 0.1	219.5	285.7	281.1	264.6	228.0
		Winkler	1.87 \pm 0.07	2.49 \pm 0.00	4.56	4.46	5.72	5.79	3.61
	0.10	Δ Cov	0.017 \pm 0.016	0.023 \pm 0.000	-0.057	-0.004	-0.017	-0.028	-0.001
		PI-Width	85.6 \pm 7.4	113.2 \pm 0.1	178.3	224.8	206.7	196.5	186.4
		Winkler	1.45 \pm 0.06	1.94 \pm 0.00	3.69	3.64	4.33	4.36	3.00
	0.15	Δ Cov	0.033 \pm 0.019	0.038 \pm 0.000	-0.061	-0.004	-0.017	-0.029	-0.001
		PI-Width	73.4 \pm 6.2	94.9 \pm 0.1	151.4	188.9	168.2	161.9	161.1
		Winkler	1.24 \pm 0.06	1.66 \pm 0.00	3.23	3.20	3.63	3.65	2.71
Ridge	0.05	Δ Cov	0.001 \pm 0.003	0.010 \pm 0.000	-0.037	-0.003	0.005	0.006	
		PI-Width	100.6 \pm 6.2	120.2 \pm 0.1	152.6	202.3	215.7	219.3	
		Winkler	1.70 \pm 0.08	1.93 \pm 0.00	3.32	3.42	3.96	3.98	
	0.10	Δ Cov	0.010 \pm 0.007	0.024 \pm 0.000	-0.045	-0.002	0.010	0.012	
		PI-Width	79.9 \pm 4.7	93.9 \pm 0.1	120.0	153.3	153.7	155.3	
		Winkler	1.35 \pm 0.06	1.52 \pm 0.00	2.60	2.68	2.95	2.96	
	0.15	Δ Cov	0.016 \pm 0.011	0.038 \pm 0.001	-0.049	-0.003	0.015	0.018	
		PI-Width	68.1 \pm 4.1	79.4 \pm 0.1	100.5	126.9	125.7	127.0	
		Winkler	1.17 \pm 0.05	1.31 \pm 0.00	2.23	2.31	2.46	2.46	
LSTM	0.05	Δ Cov	-0.001 \pm 0.001	0.003 \pm 0.000	-0.021	-0.002	-0.002	-0.001	
		PI-Width	90.7 \pm 1.9	86.1 \pm 0.0	80.8	88.8	86.8	88.1	
		Winkler	1.83 \pm 0.03	1.63 \pm 0.00	1.81	1.77	1.86	1.86	
	0.10	Δ Cov	-0.002 \pm 0.005	0.010 \pm 0.000	-0.025	-0.002	0.001	0.004	
		PI-Width	62.7 \pm 1.5	62.2 \pm 0.0	58.1	62.4	61.8	63.0	
		Winkler	1.33 \pm 0.01	1.21 \pm 0.00	1.32	1.29	1.34	1.34	
	0.15	Δ Cov	-0.002 \pm 0.010	0.017 \pm 0.000	-0.028	-0.002	0.005	0.009	
		PI-Width	49.4 \pm 1.7	50.2 \pm 0.0	46.5	49.6	49.6	50.8	
		Winkler	1.09 \pm 0.01	1.01 \pm 0.00	1.08	1.07	1.10	1.10	

Table 21: Performance of the evaluated CP algorithms on the Air Quality (25PM) dataset for the miscoverage levels $\alpha \in \{0.05, 0.10, 0.15\}$. The column FC specifies the prediction algorithm used for the experiment (Forest: Random Forest, LGBM: LightGBM, Ridge: Ridge Regression, LSTM: LSTM neural network). Bold numbers correspond to the best result for the respective metric in the experiment (PI-Width and Winkler score), given that $\Delta\text{Cov} \geq -0.25\alpha$, i.e., the specific algorithm reached at least approximate coverage (the result is grayed out otherwise). The error term represents the standard deviation over repeated runs (results without an error term are from deterministic models).

FC	α		HopCPT	SPCI	EnbPI	NexCP	CopulaCPTS	CP/CF-RNN	AdaptiveCI
Forest	0.05	Δ Cov	-0.033 \pm 0.013	-0.015 \pm 0.000	-0.065	-0.009	-0.018	-0.031	
		PI-Width	58.7 \pm 6.9	102.6 \pm 0.1	211.3	283.9	271.4	249.8	
		Winkler	1.51 \pm 0.04	2.67 \pm 0.00	5.01	4.71	6.47	6.59	
	0.10	Δ Cov	-0.024 \pm 0.017	-0.009 \pm 0.000	-0.079	-0.007	-0.025	-0.042	
		PI-Width	48.1 \pm 5.6	81.5 \pm 0.0	177.3	235.6	212.6	203.5	
		Winkler	1.12 \pm 0.05	2.02 \pm 0.00	4.31	4.05	4.94	4.98	
	0.15	Δ Cov	-0.014 \pm 0.019	-0.000 \pm 0.001	-0.084	-0.005	-0.029	-0.045	
		PI-Width	41.4 \pm 4.9	70.8 \pm 0.0	153.0	206.9	185.5	179.0	
		Winkler	0.94 \pm 0.05	1.71 \pm 0.00	3.88	3.67	4.23	4.25	
LGBM	0.05	Δ Cov	-0.031 \pm 0.014	-0.007 \pm 0.000	-0.054	-0.006	-0.020	-0.032	-0.001
		PI-Width	57.2 \pm 7.8	93.5 \pm 0.1	176.4	239.5	212.7	196.0	208.8
		Winkler	1.48 \pm 0.05	2.45 \pm 0.00	4.30	4.35	5.47	5.58	3.99
	0.10	Δ Cov	-0.021 \pm 0.019	0.002 \pm 0.000	-0.063	-0.007	-0.027	-0.042	-0.001
		PI-Width	46.8 \pm 6.0	73.3 \pm 0.0	142.1	182.2	154.5	143.9	163.3
		Winkler	1.10 \pm 0.05	1.83 \pm 0.00	3.54	3.55	4.09	4.14	3.35
	0.15	Δ Cov	-0.010 \pm 0.022	0.010 \pm 0.001	-0.066	-0.006	-0.029	-0.045	-0.001
		PI-Width	40.2 \pm 5.1	62.4 \pm 0.0	118.8	147.6	124.2	117.1	133.3
		Winkler	0.92 \pm 0.05	1.55 \pm 0.00	3.07	3.08	3.41	3.43	2.99
Ridge	0.05	Δ Cov	-0.018 \pm 0.018	-0.001 \pm 0.000	-0.043	-0.005	-0.002	-0.004	
		PI-Width	60.2 \pm 13.1	84.0 \pm 0.1	132.5	177.6	180.5	177.1	
		Winkler	1.35 \pm 0.12	1.82 \pm 0.00	3.11	3.31	3.82	3.85	
	0.10	Δ Cov	-0.005 \pm 0.026	0.011 \pm 0.000	-0.051	-0.006	-0.002	-0.004	
		PI-Width	49.3 \pm 10.6	65.5 \pm 0.0	106.2	134.3	127.4	125.3	
		Winkler	1.04 \pm 0.11	1.40 \pm 0.00	2.54	2.66	2.92	2.93	
	0.15	Δ Cov	0.008 \pm 0.032	0.021 \pm 0.000	-0.053	-0.007	-0.001	-0.003	
		PI-Width	42.6 \pm 9.3	55.6 \pm 0.0	88.7	109.7	102.5	101.6	
		Winkler	0.89 \pm 0.10	1.20 \pm 0.00	2.21	2.30	2.46	2.46	
LSTM	0.05	Δ Cov	0.005 \pm 0.005	-0.015 \pm 0.000	-0.023	-0.003	-0.015	-0.021	
		PI-Width	57.1 \pm 5.6	44.9 \pm 0.0	50.8	56.0	48.4	46.1	
		Winkler	1.19 \pm 0.08	1.29 \pm 0.00	1.33	1.27	1.39	1.40	
	0.10	Δ Cov	0.007 \pm 0.008	-0.017 \pm 0.000	-0.028	-0.003	-0.019	-0.025	
		PI-Width	40.7 \pm 4.3	32.4 \pm 0.0	35.9	38.6	34.0	32.8	
		Winkler	0.88 \pm 0.05	0.93 \pm 0.00	0.97	0.94	0.99	0.99	
	0.15	Δ Cov	0.005 \pm 0.011	-0.016 \pm 0.000	-0.029	-0.003	-0.019	-0.025	
		PI-Width	32.5 \pm 3.7	26.1 \pm 0.0	28.4	30.2	26.8	26.1	
		Winkler	0.74 \pm 0.04	0.76 \pm 0.00	0.79	0.77	0.80	0.81	

Table 22: Performance of the evaluated CP algorithms on the Sap flow dataset for the miscoverage levels $\alpha \in \{0.05, 0.10, 0.15\}$. The column FC specifies the prediction algorithm used for the experiment (Forest: Random Forest, LGBM: LightGBM, Ridge: Ridge Regression, LSTM: LSTM neural network). Bold numbers correspond to the best result for the respective metric in the experiment (PI-Width and Winkler score), given that $\Delta\text{Cov} \geq -0.25\alpha$, i.e. the specific algorithm reached at least approximate coverage (the result is grayed out otherwise). The error term represents the standard deviation over repeated runs (results without an error term are from deterministic models).

FC	α		HopCPT	SPCI	EnbPI	NexCP	CopulaCPTS	CP/CF-RNN	AdaptiveCI
Forest	0.05	Δ Cov	$-0.001^{\pm 0.014}$	$-0.002^{\pm 0.000}$	-0.047	-0.003	0.010	0.003	
		PI-Width	1333.2 ± 93.3	2193.8 ± 2.1	4264.1	7290.8	8805.8	8970.9	
		Winkler	0.38 ± 0.01	0.74 ± 0.00	1.42	1.75	2.04	2.12	
	0.10	Δ Cov	$0.009^{\pm 0.019}$	$0.007^{\pm 0.000}$	-0.042	0.000	0.014	0.005	
		PI-Width	1078.7 ± 73.7	1741.8 ± 2.4	3671.6	6137.1	7131.1	7201.5	
		Winkler	0.30 ± 0.01	0.59 ± 0.00	1.24	1.56	1.76	1.80	
	0.15	Δ Cov	$0.017^{\pm 0.024}$	$0.014^{\pm 0.001}$	-0.034	0.002	0.017	0.009	
		PI-Width	921.7 ± 61.9	1456.7 ± 2.2	3200.5	5261.8	5980.4	6062.0	
		Winkler	0.26 ± 0.01	0.50 ± 0.00	1.12	1.43	1.57	1.60	
LGBM	0.05	Δ Cov	$-0.027^{\pm 0.010}$	$-0.006^{\pm 0.000}$	-0.043	-0.006	0.006	-0.002	0.008
		PI-Width	1072.4 ± 65.8	1988.0 ± 1.0	3453.3	5737.6	6929.6	7087.5	7160.4
		Winkler	0.35 ± 0.00	0.62 ± 0.00	1.12	1.41	1.66	1.72	1.64
	0.10	Δ Cov	$-0.016^{\pm 0.013}$	$0.003^{\pm 0.000}$	-0.040	-0.003	0.006	-0.007	0.010
		PI-Width	875.5 ± 49.8	1582.3 ± 1.0	2924.1	4805.3	5588.5	5614.8	6273.5
		Winkler	0.27 ± 0.00	0.49 ± 0.00	0.96	1.25	1.43	1.46	1.50
	0.15	Δ Cov	$-0.006^{\pm 0.016}$	$0.010^{\pm 0.001}$	-0.036	-0.002	0.005	-0.012	0.010
		PI-Width	751.7 ± 41.8	1347.1 ± 1.3	2531.2	4147.4	4586.3	4544.3	5564.7
		Winkler	0.23 ± 0.00	0.42 ± 0.00	0.87	1.14	1.27	1.30	1.40
Ridge	0.05	Δ Cov	$-0.021^{\pm 0.014}$	$-0.231^{\pm 0.000}$	-0.040	-0.012	-0.174	-0.331	
		PI-Width	1971.3 ± 115.4	2539.3 ± 1.6	3595.3	11318.6	10230.3	8462.1	
		Winkler	0.54 ± 0.05	3.97 ± 0.01	1.04	2.54	3.53	8.20	
	0.10	Δ Cov	$-0.025^{\pm 0.023}$	$-0.241^{\pm 0.000}$	-0.041	-0.015	-0.251	-0.358	
		PI-Width	1639.6 ± 93.2	2060.5 ± 1.6	3117.5	10628.9	8943.3	7148.7	
		Winkler	0.46 ± 0.05	2.52 ± 0.00	0.92	2.42	3.31	5.85	
	0.15	Δ Cov	$-0.026^{\pm 0.031}$	$-0.235^{\pm 0.001}$	-0.042	-0.016	-0.292	-0.375	
		PI-Width	1427.1 ± 80.7	1792.0 ± 1.8	2775.8	10073.3	7959.3	6155.9	
		Winkler	0.42 ± 0.05	1.93 ± 0.00	0.85	2.34	3.17	4.89	
LSTM	0.05	Δ Cov	$0.001^{\pm 0.002}$	$0.000^{\pm 0.000}$	-0.018	-0.001	-0.012	-0.024	
		PI-Width	783.5 ± 9.2	897.7 ± 0.9	1020.5	1338.9	1300.1	1194.5	
		Winkler	0.25 ± 0.01	0.33 ± 0.00	0.36	0.40	0.45	0.47	
	0.10	Δ Cov	$0.004^{\pm 0.004}$	$0.004^{\pm 0.000}$	-0.019	-0.000	-0.022	-0.042	
		PI-Width	594.3 ± 7.7	628.2 ± 0.9	768.0	990.0	903.9	817.2	
		Winkler	0.19 ± 0.01	0.24 ± 0.00	0.28	0.32	0.35	0.36	
	0.15	Δ Cov	$0.005^{\pm 0.005}$	$0.006^{\pm 0.000}$	-0.019	0.002	-0.026	-0.048	
		PI-Width	489.9 ± 7.0	493.2 ± 0.5	618.2	780.6	681.5	620.4	
		Winkler	0.17 ± 0.01	0.20 ± 0.00	0.24	0.27	0.29	0.30	

Table 23: Performance of the evaluated CP algorithms and the CMAL baseline (see Appendix A.3) on the Streamflow dataset for the miscoverage levels $\alpha \in \{0.05, 0.10, 0.15\}$. Bold numbers correspond to the best result for the respective metric in the experiment (PI-Width and Winkler score), given that $\Delta\text{Cov} \geq -0.25\alpha$, i.e. the specific algorithm reached at least approximate coverage (the result is grayed out otherwise). The error term represents the standard deviation over repeated runs (results without an error term are from deterministic models).

α		HopCPT	SPCI	EmbPI	NexCP	CopulaCPTS	CP/CF-RNN	CMAL
0.05	ΔCov	$-0.002^{\pm 0.022}$	$0.013^{\pm 0.000}$	-0.042	-0.001	0.003	0.006	$-0.004^{\pm 0.004}$
	PI-Width	$1.91^{\pm 0.20}$	$2.57^{\pm 0.00}$	2.53	3.23	3.44	3.63	$2.4^{\pm 0.08}$
	Winkler	$1.05^{\pm 0.03}$	$1.38^{\pm 0.00}$	1.91	1.80	1.93	1.94	$0.78^{\pm 0.01}$
0.10	ΔCov	$0.001^{\pm 0.041}$	$0.027^{\pm 0.000}$	-0.054	-0.000	0.005	0.009	$-0.004^{\pm 0.008}$
	PI-Width	$1.39^{\pm 0.17}$	$1.58^{\pm 0.00}$	1.55	1.94	1.99	2.08	$1.90^{\pm 0.06}$
	Winkler	$0.79^{\pm 0.03}$	$0.91^{\pm 0.00}$	1.27	1.21	1.28	1.29	$0.63^{\pm 0.01}$
0.15	ΔCov	$0.003^{\pm 0.056}$	$0.038^{\pm 0.000}$	-0.061	0.001	0.005	0.009	$-0.006^{\pm 0.011}$
	PI-Width	$1.11^{\pm 0.15}$	$1.17^{\pm 0.00}$	1.12	1.39	1.39	1.45	$1.60^{\pm 0.05}$
	Winkler	$0.66^{\pm 0.03}$	$0.71^{\pm 0.00}$	0.98	0.95	0.99	1.00	$0.55^{\pm 0.03}$